The Astrophysical Journal, 983:10 (22pp), 2025 April 10 https://doi.org/10.3847/1538-4357/adb430

The Qz5 Survey. I. How the H I Mass Density of the Universe Evolves with Cosmic Time

Grecco A. Oyarzún[1], Marc Rafelski[1,2], Lise Christensen[3], Fiona Ozyurt[4,5], Regina A. Jorgenson[4], M. Neeleman[6], Michele Fumagalli[7,8], J. Xavier Prochaska[9,10,11], G. Worseck[12], M. E. Wisz[4,13], George D. Becker[14], and Sebastián López[15]

[1] Department of Physics and Astronomy, Johns Hopkins University, Baltimore, MD 21218, USA; goyarzu1@jhu.edu
[2] Space Telescope Science Institute, 3700 San Martin Drive, Baltimore, MD 21218, USA
[3] Cosmic Dawn Center, Niels Bohr Institute, University of Copenhagen, Jagtvej 128, 2200-N Copenhagen, Denmark
[4] Maria Mitchell Observatory, 4 Vestal Street, Nantucket, MA 02554, USA
[5] Department of Physics, Southern Connecticut State University, New Haven, CT 06515, USA
[6] National Radio Astronomy Observatory, 520 Edgemont Road, Charlottesville, VA 22903, USA
[7] Dipartimento di Fisica G. Occhialini, Università degli Studi di Milano-Bicocca, Piazza della Scienza 3, I-20126 Milano, Italy
[8] INAF—Osservatorio Astronomico di Trieste, via G. B. Tiepolo 11, I-34143 Trieste, Italy
[9] Department of Astronomy & Astrophysics, UCO/Lick Observatory, University of California, 1156 High Street, Santa Cruz, CA 95064, USA
[10] Kavli Institute for the Physics and Mathematics of the Universe (Kavli IPMU), 5-1-5 Kashiwanoha, Kashiwa, 277-8583, Japan
[11] Division of Science, National Astronomical Observatory of Japan, 2-21-1 Osawa, Mitaka, Tokyo 181-8588, Japan
[12] Institut für Physik und Astronomie, Universität Potsdam, Karl-Liebknecht-Straße 24/25, D-14476 Potsdam, Germany
[13] Department of Physics, University of California, Merced, CA 95343, USA
[14] Department of Physics & Astronomy, University of California, Riverside, CA, 92521, USA
[15] Departamento de Astronomía, Universidad de Chile, Casilla 36-D, Santiago, Chile
Received 2024 October 10; revised 2025 February 6; accepted 2025 February 6; published 2025 April 1

Abstract

We report that the neutral hydrogen (H I) mass density of the Universe ($\rho_{\rm H\,I}$) increases with cosmic time since $z \sim 5$, peaks at $z \sim 3$, and then decreases toward $z \sim 0$. This is the first result of Qz5, our spectroscopic survey of 63 quasars at $z \gtrsim 5$ with VLT/X-SHOOTER and Keck/ESI aimed at characterizing intervening H I gas absorbers at $z \sim 5$. The main feature of Qz5 is the high resolution ($R \sim 7000$–9000) of the spectra, which allows us to (1) accurately detect high column density H I gas absorbers in an increasingly neutral intergalactic medium at $z \sim 5$ and (2) determine the reliability of previous $\rho_{\rm H\,I}$ measurements derived with lower resolution spectroscopy. We find five intervening damped Lyα absorbers (DLAs) at $z > 4.5$, which corresponds to the lowest DLA incidence rate ($0.034^{0.05}_{0.02}$) at $z \gtrsim 2$. We also measure the lowest $\rho_{\rm H\,I}$ at $z \gtrsim 2$ from our sample of DLAs and subDLAs, corresponding to $\rho_{\rm H\,I} = 0.56^{0.82}_{0.31} \times 10^8\,M_\odot\ {\rm Mpc}^{-3}$ at $z \sim 5$. Taking into account our measurements at $z \sim 5$ and systematic biases in the DLA detection rate at lower spectral resolutions, we conclude that $\rho_{\rm H\,I}$ doubles from $z \sim 5$ to $z \sim 3$. From these results emerges a qualitative agreement between how the cosmic densities of H I gas mass, molecular gas mass, and star formation rate build up with cosmic time.

Unified Astronomy Thesaurus concepts: Neutral hydrogen clouds (1099); Damped Lyman-alpha systems (349); Intergalactic clouds (809); Intergalactic gas (812); Extragalactic astronomy (506); Quasar absorption line spectroscopy (1317); Intergalactic medium (813); Circumgalactic medium (1879); Observational cosmology (1146); Galaxies (573); Cosmology (343)

1. Introduction

The gas within and around galaxies is a critical component in our models of galaxy formation and evolution. The exchange of gas between galaxies and their circumgalactic medium (CGM)—i.e., the baryon cycle—is necessary to explain how galaxies modulate their star formation, how they transition into quiescence, and how their chemical composition (both stellar and gaseous) evolves with cosmic time (J. Tumlinson et al. 2017). Particularly responsible for triggering star formation is neutral hydrogen (H I). Because of its low temperatures ($T < 10^4$ K), H I can be efficiently accreted onto galaxies and ultimately form molecular gas (H_2) where high enough densities for star formation are achieved (M. R. Krumholz et al. 2011; S. C. O. Glover & P. C. Clark 2012; M. R. Krumholz 2012). These processes are imprinted in observations of nearby galaxies, with star-forming galaxies often showing evidence of high H I mass surface densities (e.g., R. C. Kennicutt 1998; R. C. Kennicutt & N. J. Evans 2012; F. Fraternali et al. 2002; R. Sancisi et al. 2008).

Key for the formation of this picture have been observations of gas in emission (M. P. Haynes & R. Giovanelli 1984; M. A. Zwaan et al. 2005; F. Bigiel et al. 2008; B. Catinella et al. 2013, 2018; M. P. Haynes et al. 2018). The H I emission line at 21 cm has been exploited with great success to estimate the star formation efficiency, size, and kinematics of H I disks in the nearby Universe (e.g., A. Begum et al. 2008; A. K. Leroy et al. 2008; F. Walter et al. 2008; J. Wang et al. 2016; N. Yu et al. 2022; A. Sharma et al. 2023; J. Dou et al. 2024). Unfortunately, the 21 cm line is too weak to directly measure with current observatories in individual galaxies beyond $z > 0.4$ (X. Fernández et al. 2016; H. Xi et al. 2024) and through stacking beyond $z \sim 1.5$ (A. Chowdhury et al. 2020; A. Chowdhury et al. 2021; A. Chowdhury et al. 2022). Thus, we remain unable to constrain the properties of H I through the peak of cosmic star formation history in emission ($z \gtrsim 2$; P. Madau & M. Dickinson 2014).

To study H I at $z = 2$–5, we can instead utilize observations of H I in absorption. The principle behind H I absorption

studies is that neutral gas throughout the Universe absorbs and/or scatters most of the UV radiation field. Primary examples of this technique are the absorption signatures produced by high-column density H I gas in the spectra of background quasars (QSOs), known as a damped Lyα absorbers (DLAs; A. M. Wolfe et al. 2005). DLAs provide a unique laboratory for studying H I gas at intermediate and high redshifts, enabling measurements of the dust depletion, molecular fraction, gas temperature, gas kinematics, and metal enrichment of H I gas reservoirs out to $z \sim 5.5$ (e.g., J. X. Prochaska & A. M. Wolfe 1997; M. Rafelski et al. 2012, 2014; J. X. Prochaska et al. 2013; M. Neeleman et al. 2013, 2015; N. H. M. Crighton et al. 2015; P. Noterdaeme et al. 2015, 2023; S. A. Balashev et al. 2017; J. Bolmer et al. 2019; F. Combes & N. Gupta 2024). Moreover, DLAs are also regularly exploited to search for the galaxies associated with H I gas reservoirs out to $z \sim 4.5$ (i.e., H I-selected galaxies; e.g., P. Møller & S. J. Warren 1993; H.-W. Chen & K. M. Lanzetta 2003; J. P. U. Fynbo et al. 2010; J. K. Krogager et al. 2017; M. Neeleman et al. 2017; R. Mackenzie et al. 2019; M. Neeleman et al. 2019; N. Kanekar et al. 2020; B. Kaur et al. 2022a; E. K. Lofthouse et al. 2023; G. A. Oyarzún et al. 2024).

Because of their high $N_{\rm H\,I}$, DLAs are thought to account for the bulk (>70%) of the H I mass from $z = 2$ (e.g., J. M. O'Meara et al. 2007; T. Zafar et al. 2013) out to at least $z \sim 4$ (T. A. M. Berg et al. 2019). This makes the DLAs a convenient probe for the cosmic H I mass density ($\rho_{\rm H\,I}$). This quantity garners interest from both observational and theoretical work (e.g., J. X. Prochaska & A. M. Wolfe 2009; P. Noterdaeme et al. 2009, 2012; A. Rahmati et al. 2015; G. Popping et al. 2014) because it captures the availability of fuel for star formation throughout cosmic time and because it reflects the efficiency with which gas is turned into stars in the Universe (e.g., F. Walter et al. 2020).

While semianalytic models and some simulations predict a rise and fall of $\rho_{\rm H\,I}$ similar to the cosmic star formation rate density (e.g., R. S. Somerville et al. 2001; G. Popping et al. 2014; R. Davé et al. 2019), the interpretation of most DLA surveys to date is that $\rho_{\rm H\,I}$ is a steadily increasing function with redshift out to at least $z \sim 5$ (e.g., J. X. Prochaska & A. M. Wolfe 2009; P. Noterdaeme et al. 2012; N. H. M. Crighton et al. 2015), with the functional form $\rho_{\rm H\,I} \propto (1+z)^{0.57}$ providing a reasonable description of the observations (C. Péroux & J. C. Howk 2020).

To better understand the tension between simulations and observations in how $\rho_{\rm H\,I}$ evolves with redshift, we need to establish if there are any systematic biases affecting the different techniques employed for measuring $\rho_{\rm H\,I}$. Relevant to this point is that attaining large, statistically significant samples of quasars (QSOs) at $z \gtrsim 5$ is difficult due to the decrease in both the spatial density and brightness of QSOs with redshift. It is because of these challenges that DLA surveys designed to measure $\rho_{\rm H\,I}$ at $z \gtrsim 3.5$ often turn to low-resolution ($R \sim 2000$) and low signal-to-noise ratio (S/N $\lesssim$ 5) spectroscopy (J. X. Prochaska & A. M. Wolfe 2009; S. Bird et al. 2017; M.-F. Ho et al. 2020). Even at higher S/N (S/N $\sim$ 15) and after careful simulations to account for false positives and incompleteness at low resolutions, N. H. M. Crighton et al. (2015) still found the DLA incidence rate to remain highly uncertain for $R \sim 1300$ data. This is because the intergalactic medium (IGM) becomes increasingly opaque as redshift increases, making spectroscopic identification of DLAs toward $z \gtrsim 3.5$ more challenging than at $z \sim 2$–3 (P. Noterdaeme et al. 2012; M. Rafelski et al. 2012). Therefore, our understanding of how $\rho_{\rm H\,I}$ evolves with redshift would greatly benefit from a high-resolution spectroscopic survey of QSOs at $z \gtrsim 3.5$.

In this paper, we present Qz5[16]: a high-resolution ($R \sim 7000$–9000) spectroscopic survey of 63 bright QSOs at $z \gtrsim 5$ that was specifically designed to measure (1) $\rho_{\rm H\,I}$ at $z \sim 5$ and (2) the metallicity of the Universe at $z \sim 5$ (M. E. Wisz et al. 2025, in preparation). The high-resolution spectroscopic observations were carried with either the Keck Echellette Spectrograph and Imager (ESI; A. I. Sheinis et al. 2002) or the Very Large Telescope (VLT)/X-SHOOTER (J. Vernet et al. 2011). This paper is structured as follows. In Section 2, we introduce our sample and describe the observations. Our methodology to identify DLAs and to measure $\rho_{\rm H\,I}$ is presented in Section 3. Our results are outlined in Section 4. We conclude in Section 5 and summarize in Section 6. We adopt a ΛCDM cosmology with $\Omega_\Lambda = 0.7$, $\Omega_m = 0.3$, and $H_0 = 70\,{\rm km\,s^{-1}\,Mpc^{-1}}$. All cosmic mass densities are reported in comoving units and all magnitudes are reported in the AB system (J. B. Oke & J. E. Gunn 1983).

2. The Qz5 Survey

2.1. Sample

The sample of Qz5 is composed of two different subsets of QSOs at $z \sim 5$. The first subset is composed of 22 QSOs from the Sloan Digital Sky Survey (SDSS) Baryon Oscillation Spectroscopic Survey (BOSS; DR9 and DR10; C. P. Ahn et al. 2014; I. Pâris et al. 2017) that were observed with Keck/ESI. Because the original goal of the Keck program was to measure the metallicity of DLAs at $z > 4.7$, some of these 22 QSOs were originally selected based on the preidentification of DLAs in the BOSS spectra (P. Noterdaeme et al. 2012). However, early in the program it became apparent that DLA candidates identified in the P. Noterdaeme et al. (2012) catalog are false positives due to (1) the increasing density of the Lyα forest and (2) the low S/N of BOSS spectra for QSOs at these redshifts (M. Rafelski et al. 2014). Hence, the program pivoted to targeting QSOs from BOSS at $4.7 < z < 5.7$ based solely on redshift and magnitude (i.e., without any DLA preidentification). Since none of the nonproximate DLA candidates identified in P. Noterdaeme et al. (2012) are real DLAs or subDLAs (M. Rafelski et al. 2014), we treat all 22 QSOs as an unbiased sample. The properties of these QSOs observed with Keck/ESI are presented in Table 1.

The second subset of QSOs is based on optical and mid-infrared photometric selection and low spectral resolution follow-up of targets originally identified in the Wide-field Infrared Survey Explorer (WISE; E. L. Wright et al. 2010), as described in F. Wang et al. (2016) and J. Yang et al. (2016). We observed 41 of these QSOs with VLT/X-SHOOTER (J. Vernet et al. 2011) based on their magnitudes and redshifts. The properties of these QSOs are also summarized in Table 1. In total, the sample of this work is composed of 63 QSOs at $4.7 < z < 5.7$, and is considered unbiased with regard to the presence of DLAs.

[16] DOI: 10.5281/zenodo.14825981.

Table 1
QSO Sample

QSO	R.A.	Decl.	m_z	z_{em}	Instrument	t_{exp} (s)	S/N[1]	S/N[2]
J0007+0041	00:07:49.17	00:41:19.62	19.84	4.76	ESI	1800	2.2	26.1
J0017-1000	00:17:14.67	-10:00:55.41	19.61	4.99	XSH	2400	2.1	37.9
J0025-0145	00:25:26.84	-01:45:32.50	17.86	5.06	XSH	600	2.6	48.1
J0054-0109	00:54:21.43	-01:09:21.67	19.57	5.03	ESI	3600	3.5	26.0
J0108+0711	01:08:06.59	07:11:21.27	19.58	5.54	XSH	2400	2.1	31.1
J0115-0253	01:15:46.27	-02:53:12.23	19.59	5.06	XSH	1800	1.6	27.2
J0116+0538	01:16:14.31	05:38:17.59	19.27	5.33	XSH	1800	2.3	46.0
J0131-0321	01:31:27.35	-03:21:00.08	18.00	5.19	XSH	600	2.0	30.6
J0155+0415	01:55:33.28	04:15:06.74	19.28	5.33	XSH	2400	2.3	30.8
J0216+2304	02:16:24.16	23:04:09.47	19.50	5.21	XSH	1800	1.5	26.3
J0221-0342	02:21:12.62	-03:42:52.31	19.56	5.01	XSH	1800	2.4	50.8
J0241+0435	02:41:52.92	04:35:53.45	19.56	5.18	XSH	1800	1.7	43.8
J0251+0333	02:51:21.33	03:33:17.39	19.15	4.99	XSH	1200	3.5	53.8
J0306+1853	03:06:42.51	18:53:15.82	17.66	5.33	XSH	1200	6.6	58.2
J0338+0021	03:38:29.32	00:21:56.23	19.76	4.99	XSH	2400	3.3	29.2
J0747+1153	07:47:49.18	11:53:52.44	18.31	5.25	XSH	1200	2.2	64.1
J0756+4104	07:56:18.14	41:04:08.59	19.90	5.09	ESI	1800	2.4	18.9
J0812+0440	08:12:48.82	04:40:56.57	19.83	5.31	XSH	4980	2.1	67.1
J0835+0537	08:35:54.37	05:37:53.04	19.78	5.06	XSH	4980	2.2	30.9
J0846+0800	08:46:27.84	08:00:51.72	19.64	4.99	XSH	2400	1.7	22.5
J0854+2056	08:54:30.37	20:56:50.84	19.34	5.17	XSH	1800	2.0	53.7
J0902+0851	09:02:45.76	08:51:15.90	19.89	5.21	XSH	2400	1.4	51.4
J0957+0519	09:57:27.87	05:19:05.26	19.64	5.18	ESI	5400	2.4	40.4
J0957+0610	09:57:07.68	06:10:59.55	18.88	5.16	XSH	1200	3.6	30.6
J0957+1016	09:57:12.20	10:16:18.58	19.63	5.12	XSH	2400	0.8	20.8
J1004+2025	10:04:44.31	20:25:20.03	19.69	5.00	XSH	2400	1.6	23.2
J1004+4045	10:04:49.59	40:45:54.00	19.78	4.89	ESI	3300	2.7	32.7
J1022+2252	10:22:10.04	22:52:25.35	19.29	5.48	XSH	2400	2.0	63.1
J1028+0746	10:28:33.46	07:46:18.94	19.93	5.17	ESI	1800	2.2	27.0
J1146+4037	11:46:57.79	40:37:08.59	19.30	4.98	ESI	5400	7.2	69.2
J1147-0109	11:47:06.42	-01:09:58.37	19.28	5.25	XSH	1800	1.6	22.4
J1200+1817	12:00:55.62	18:17:32.91	19.24	4.98	XSH	1800	4.4	41.6
J1204-0021	12:04:41.73	-00:21:49.54	18.97	5.08	ESI	1200	3.4	26.7
J1245+3822	12:45:15.46	38:22:47.51	19.43	4.95	ESI	1800	3.2	32.0
J1332+2208	13:32:57.44	22:08:35.87	19.23	5.12	XSH	1200	3.6	52.6
J1335-0328	13:35:56.24	-03:28:38.29	18.97	5.68	XSH	1200	1.3	44.0
J1341+3510	13:41:54.02	35:10:05.80	19.46	5.25	ESI	2600	1.9	37.4
J1345+2329	13:45:26.62	23:29:49.30	18.78	5.04	ESI	1200	1.8	30.2
J1418+3142	14:18:39.99	31:42:44.07	19.23	4.91	ESI	1800	2.7	23.5
J1421+3433	14:21:03.83	34:33:32.00	18.85	4.94	ESI	2700	2.4	25.5
J1423+1303	14:23:26.04	13:02:57.55	19.43	5.03	XSH	1800	3.5	38.1
J1436+2132	14:36:05.00	21:32:39.26	19.28	5.22	XSH	2400	1.8	32.4
J1443+0605	14:43:52.94	06:05:33.16	19.93	4.91	ESI	1800	1.0	19.8
J1443+3623	14:43:50.67	36:23:15.18	19.47	5.37	ESI	2400	1.7	35.2
J1523+3347	15:23:45.69	33:47:59.41	20.16	5.35	ESI	1800	0.9	21.4
J1534+1327	15:34:59.76	13:27:01.43	20.57	5.05	ESI	1800	0.8	44.2
J1536+1437	15:36:27.10	14:37:17.12	19.87	4.91	ESI	1800	1.5	26.2
J1601-1828	16:01:11.17	-18:28:35.07	19.54	5.03	XSH	1800	1.4	25.4
J1614+2059	16:14:47.04	20:59:02.85	19.74	5.06	ESI	1200	2.5	19.0
J2201+0302	22:01:06.63	03:02:07.70	18.97	5.06	XSH	1200	3.0	29.4
J2202+1509	22:02:26.77	15:09:52.37	18.55	5.07	XSH	960	2.4	35.3
J2207-0416	22:07:10.13	-04:16:56.22	19.10	5.51	XSH	1200	1.1	44.7
J2216+0013	22:16:44.02	00:13:48.14	19.93	5.01	ESI	1200	1.8	19.3
J2220-0101	22:20:18.50	-01:01:47.08	20.13	5.62	ESI	2400	0.7	24.1
J2225+0330	22:25:14.38	03:30:12.52	19.64	5.25	XSH	2400	0.9	21.7
J2226-0618	22:26:12.42	-06:18:07.35	18.77	5.09	XSH	600	1.5	24.5
J2228-0757	22:28:45.14	-07:57:55.30	19.38	5.15	XSH	3600	1.5	41.7
J2312+0100	23:12:16.45	01:00:51.58	20.88	5.08	ESI	2400	0.7	29.9
J2325-0553	23:25:36.64	-05:53:28.42	19.19	5.20	XSH	1200	1.4	21.7
J2330+0957	23:30:08.71	09:57:43.73	19.75	5.25	XSH	2400	1.3	17.0
J2344+1653	23:44:33.50	16:53:16.58	18.60	5.00	XSH	600	1.9	25.5
J2351-0459	23:51:24.31	-04:59:07.30	19.59	5.26	XSH	2400	1.9	30.7
J2358+0634	23:58:24.05	06:34:37.48	19.52	5.27	XSH	2400	2.7	30.3

Note. Column (1): QSO name. Column (2): R.A. Column (3): decl. Column (4): QSO z-band magnitude from SDSS. Column (5): QSO redshift measured by Qz5. Column (6): instrument. Column (7): exposure time. Column (8): median S/N per pixel in the Lyα forest at the wavelengths of the search path. Column (9): peak S/N per pixel in the vicinity of the Lyα emission from the QSO.

2.2. Observations and Data

The Keck/ESI data were obtained in 2013 January, 2013 May, and 2013 August with the $\sim 0\farcs75$ slit. The seeing varied between $0\farcs6$ and $1\farcs1$. This configuration corresponds to a spectral resolution of $R \sim 7000$, which is equivalent to $\sim 44\ \mathrm{km\ s^{-1}}$ (FWHM). The Keck/ESI data were dithered along the slit with a three-point dither pattern to decrease the effects of fringing, although not all observations included all three dither positions.

The VLT/X-SHOOTER data were obtained in service mode through the programs 098.A-0111 and 0100.A-0243 (PI: M. Rafelski). The observations were conducted between 2017 October and 2018 March with the $0\farcs9$ slit in the VIS arm and $0\farcs6$ slit in the NIR arm. For the VIS ($\lambda \sim 0.5$–$1\ \mu$m) arm, this corresponds to $R \sim 8900$ and $\sim 34\ \mathrm{km\ s^{-1}}$ (FWHM). For the NIR arm ($\lambda \sim 1$–$2.5\ \mu$m), the data feature $R \sim 8100$, which is equivalent to $\sim 37\ \mathrm{km\ s^{-1}}$ (FWHM). We used 1x2 binning for the VIS arm data, which still sufficiently samples the PSF with 3 pixels per resolution element.

2.3. Data Reduction

To process the Keck/ESI data, we turned to the software `XIDL` developed by J.X. Prochaska. We utilized the package `ESIRedux` with optimal extraction (J. X. Prochaska et al. 2003) that follows the same methodology described in M. Rafelski et al. (2012).

To process the VLT/X-SHOOTER data, we used a set of custom built IDL software codes written by G. Becker. Previous testing of these codes on quasar spectra from the XQ-100 survey (S. López et al. 2016) revealed improved sky subtraction over the standard ESO pipeline (A. Modigliani et al. 2010), especially for the near-infrared spectra. One of the main differences between these two pipelines is the nodding strategy. The IDL routine used in this work does not implement nodding for the subtraction of the sky background, avoiding a factor of $\sqrt{2}$ increase in the noise during reduction.

Strong telluric absorption lines affect both the optical and near-infrared spectral ranges. After each of the quasar observations, VLT/X-SHOOTER also carried out associated observations of a hot B-type star to allow us to model the strengths of the atmospheric absorption lines. To correct for the pressure, temperature, and airmass-dependent strengths, we used the ESO `Molecfit` tool (A. Smette et al. 2015) to model the transmission in the telluric standard star spectra and correct the extracted quasar spectra for the atmospheric absorption lines.

The final one-dimensional spectra were extracted, combined, and flux calibrated using observations of spectrophotometric standard stars obtained during the night of the science observations. Wavelength calibration corrected all spectra into vacuum, heliocentric frame. We found a systematic wavelength shift in the wavelength calibrated VLT/X-SHOOTER spectra.[17] We determined the magnitude of this wavelength shift through a cross-correlation between the reduced spectra and the Cerro Paranal Advanced Sky Model.[18] All shifts were found to be within $\lesssim 1$ Å and were used to correct the wavelength solution of the reduced data products. This process will be outlined in greater detail in a companion paper that focuses on the metal line absorption (M. E. Wisz et al. 2025, in preparation). Appendix A provides a hyperlink to download the data and shows the spectra for the 63 QSOs.

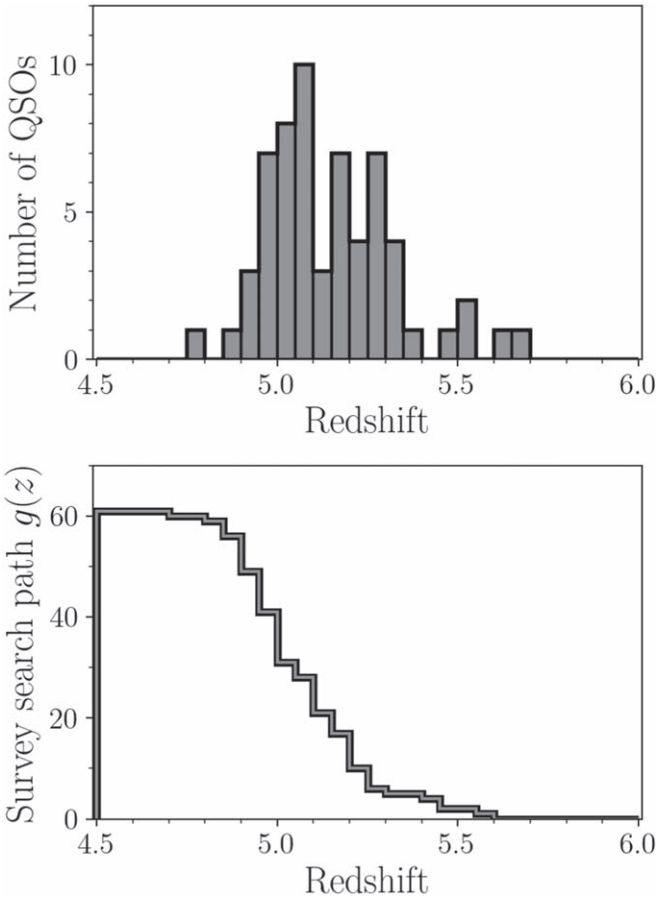

Figure 1. The QSO sample comprising Qz5. Top panel: histogram of the redshifts of the 63 QSOs in our sample. We carried out high-resolution spectroscopic observations of these QSOs in order to identify DLAs and constrain $\rho_{\mathrm{H\,I}}$ at $z \sim 5$. Bottom panel: number of sightlines available for the identification of DLAs (i.e., $g(z)$, the survey search path of Qz5) as a function of redshift. The search path remains high out to $z \sim 4.9$ before dropping toward $z \sim 5.5$.

2.4. Emission Redshifts and Survey Search Path

We utilized the reduced spectra to remeasure the emission redshifts of the QSOs. To this end, we designed an algorithm that maximizes the cross-correlation between the observed spectra and an estimate of the QSO continuum obtained with `Quasar Factor Analysis` (Z. Sun et al. 2023). The QSO redshifts are presented in Table 1 and the redshift distribution of the sample is shown in Figure 1. The typical uncertainties on the redshifts are $z_{\mathrm{err}} = 0.05$, and we found our redshifts and those measured by SDSS and/or F. Wang et al. (2016) to be within $\Delta z = 0.08$ in all cases.

In Figure 1, we also show the survey search path or $g(z)$ of Qz5. Because all 63 quasars in Qz5 have emission redshifts $z_{\mathrm{em}} > 4.7$, the available path length between $z \sim 4.5$ and 4.7 is 63. This path length decreases toward lower and higher redshift because fewer QSOs are available to search for Lyα absorbers. Therefore, and because the goal of our study is to constrain $\rho_{\mathrm{H\,I}}$ at $z \sim 5$, we limit our analysis to the redshift range $z = 4.5$–5.6.

[17] https://www.eso.org/sci/facilities/paranal/instruments/xshooter/doc/XS_wlc_shift_150615.pdf

[18] https://www.eso.org/observing/etc/bin/gen/form?INS.MODE=swspectr+INS.NAME=SKYCALC

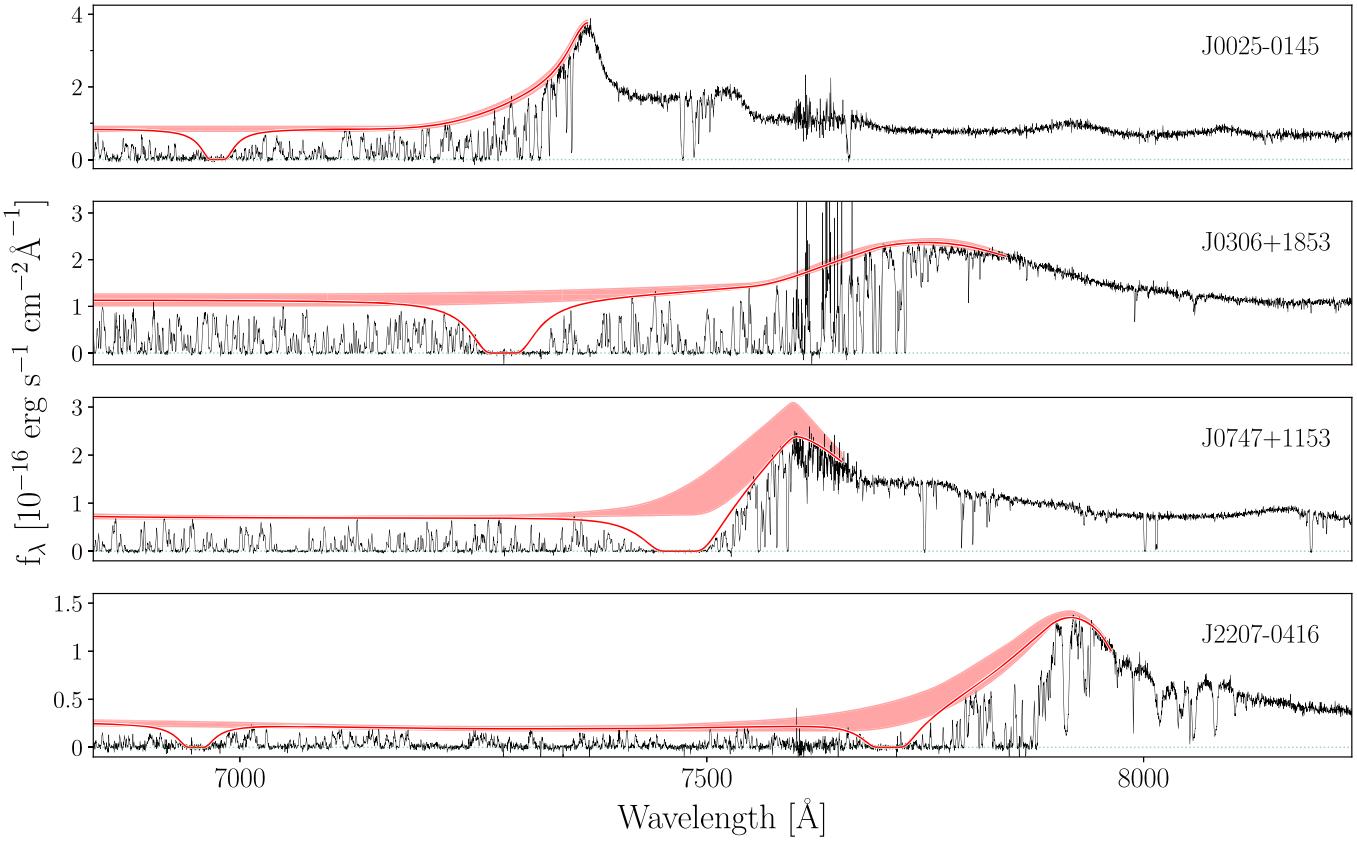

Figure 2. Spectra of the four QSOs featuring the five DLAs detected in Qz5. The QSO identifiers are shown in the top right-hand corner of every panel. All these QSOs were observed with VLT/X-SHOOTER. Also plotted are the estimated QSO continuum fluxes blueward of Lyα (red shading) and the associated Voigt profile fits to the DLAs used to determine their $N_{\rm H\,I}$ (red lines). Details on how these continua were determined are presented in Section 3.1.

It is apparent in Figure 1 that $g(z)$ of Qz5 is at its highest out to $z \sim 4.9$, with a rapid decrease as we approach $z \sim 5.5$.

3. Methodology

3.1. Analysis

Because of the high spectral resolution, adequate S/N, and the moderate sample size of our data set, we were able to search for DLAs and subDLAs through visual inspection without the need for an automated algorithm. Effectively, we selected all regions with widths greater than 10 Å in the Lyα forest of every QSO that are consistent with zero flux. Our search yielded a sample of 39 high-$N_{\rm H\,I}$ absorber candidates in the 63 QSOs.

Distinguishing between DLAs and subDLAs (i.e., measuring $N_{\rm H\,I}$ for all candidates) requires estimation of the QSO continuum blueward of the Lyα emission peak. We note that the Lyα forest is very dense at these redshifts, and thus the standard practice of only fitting $N_{\rm H\,I}$ to the peaks of the Lyα forest could slightly overestimate $N_{\rm H\,I}$. Therefore, we fit two continua in the Lyα forest per target. The first fits were set to closely align with the peaks of the Lyα forest (as typically done; e.g., M. Rafelski et al. 2012). To account for possible Lyα absorption, the second fits were set to higher flux density values (typically by 10%–20%). These fits aim to encompass the maximum QSO continuum level allowed by template QSO spectra at lower redshifts, including the Lyα emission peak (see Figure 2 for examples). The two continuum fits were averaged to determine the best continuum estimate, which was then used to normalize the QSO spectrum for the characterization of H I absorbers.

This best continuum estimate was utilized to visually determine the best-fit $N_{\rm H\,I}$ (to which we will refer as simply $N_{\rm H\,I}$) for all candidate absorbers. The uncertainties (to which we will refer as $\Delta N_{\rm H\,I}$) were determined by visually fitting the DLA at both the lower and higher continuum levels to fully encompass the uncertainty on $N_{\rm H\,I}$. We note that $\Delta N_{\rm H\,I}$ is dominated by the uncertainties on the QSO continuum, and thus our uncertainties are conservative. Of the 39 high-$N_{\rm H\,I}$ absorbers, eight were found to satisfy the DLA column density threshold (i.e., $N_{\rm H\,I} \geqslant 10^{20.3}$ cm^{-2}) and 31 were best classified as subDLAs (i.e., $10^{19} \leqslant N_{\rm H\,I}$ [cm^{-2}] $< 10^{20.3}$). These eight DLAs were fitted by three authors independently (G. A. Oyarzún, M. Rafelski, and F. Ozyurt), and the recovered values for $N_{\rm H\,I}$ were within $\Delta N_{\rm H\,I}$ in every case.

The DLA sample was subject to further processing and analysis, including continuum fitting redward of Lyα emission from the QSO. The best-fit continuum, which was determined with the `lt_continuumfit` routine of the `linetools` package[19] (J. X. Prochaska et al. 2016) was used to normalize the QSO spectrum for the characterization of metal line absorption and subsequent absorption redshift determination. A wide range of metal lines was used in this process, in most cases including O I λ1302, Si II λ1304, C II λ1334, Si II λ1526, and Fe II λ1608. We then used the routine `pyigm_fitdla` of the `linetools` package to derive redshifts from the metal lines for the eight DLAs. No DLA candidates without associated metal lines were identified. The properties of the eight DLAs found are summarized in Table 2.

[19] https://zenodo.org/records/168270

Table 2
DLAs Identified in Qz5

QSO	R.A.	Decl.	z_{em}	z_{abs}	Notes	$\log N_{\rm H\,I}$ ($\rm cm^{-2}$)
J0007+0041	00:07:49.17	00:41:19.62	4.76	4.7330	N: Proximate DLA	20.6 ± 0.3
J0025-0145	00:25:26.84	-01:45:32.50	5.06	4.7389	Y: DLA	20.3 ± 0.15
J0306+1853	03:06:42.51	18:53:15.82	5.33	4.9866	Y: DLA	20.9 ± 0.15
J0747+1153	07:47:49.18	11:53:52.44	5.25	5.1447	Y: DLA	21.1 ± 0.25
J1345+2329	13:45:26.62	23:29:49.30	5.04	5.0060	N: Proximate DLA	21.1 ± 0.1
J1436+2132	14:36:05.00	21:32:39.26	5.22	5.1780	N: Proximate DLA	20.7 ± 0.25
J2207-0416	22:07:10.13	-04:16:56.22	5.51	4.7220	Y: DLA	20.4 ± 0.2
...	...	...	...	5.3374	Y: DLA	20.8 ± 0.15

Note. Column (1): QSO identifier. Column (2): R.A. Column (3): decl. Column (4): emission redshift. Column (5): absorption redshift. Column (6): notes. Column (7): $\log N_{\rm H\,I}$.

The redshifts were used to exclude all proximate absorbers—i.e., all absorbers within $<5000\,{\rm km\,s^{-1}}$ of Lyα emission from the QSO—because they can no longer be considered an intervening gas cloud that is not associated with the QSO (J. X. Prochaska et al. 2008; S. L. Ellison et al. 2010, 2011). Three of the eight DLAs and two of the 31 subDLAs were found to be proximate. After their removal from the sample, we obtained a total of five intervening DLAs and 29 intervening subDLAs. The $N_{\rm H\,I}$ fits for the DLAs are shown in Figure 2, and some of the metal lines used to determine their redshifts are plotted in Figure 3. All absorbers (i.e., both DLAs and subDLAs) that were identified in this analysis are presented in Appendix B.

3.2. Formalism for Measuring $\rho_{H\,I}$

We can use our data set of detected and characterized DLAs to constrain the H I column density distribution. This distribution function is typically denoted as $f(N_{\rm H\,I}, X)$, where $N_{\rm H\,I}$ is the H I column density and X is the absorption distance (J. N. Bahcall & P. J. E. Peebles 1969; K. M. Lanzetta et al. 1991; A. M. Wolfe et al. 2005). The latter is related to the geometry of the Universe by the relation

$$dX = \frac{H_0}{H(z)}(1+z)^2 dz. \quad (1)$$

In practice, we measured $f(N_{\rm H\,I}, X)$ in bins of $N_{\rm H\,I}$ and X, i.e.,

$$f(N_{\rm H\,I}, X) = \frac{\rm N_{DLA}(N_{H\,I}, N_{H\,I} \pm \delta N_{H\,I}/2)}{\delta X}, \quad (2)$$

where $\delta N_{\rm H\,I}$ and δX represent the width of the bins in $N_{\rm H\,I}$ and X, respectively. $N_{\rm DLA}$ denotes the number of DLAs at the given $N_{\rm H\,I}$ and X bin (J. X. Prochaska et al. 2005).

Measurements of $f(N_{\rm H\,I}, X)$ can be utilized to infer $\ell_{\rm DLA}(X)$, the DLA incidence rate. In equation form,

$$\ell_{\rm DLA}(X)\,dX = \frac{dN_{\rm H\,I}}{dX}\,dX = \int_{N_{\rm min}}^{\infty} f(N_{\rm H\,I}, X)\,dN_{\rm H\,I}\,dX, \quad (3)$$

where $N_{\rm min}$ corresponds to the lower limit for the column density of DLAs, i.e., $N_{\rm min} = 10^{20.3}\,{\rm cm^{-2}}$. By definition, the DLA incidence rate captures the total number of high-$N_{\rm H\,I}$ absorbers in the Universe at a given redshift. Because of this, $\ell_{\rm DLA}(X)$ is independent of systems with $N_{\rm H\,I} < 10^{20.3}\,{\rm cm^{-2}}$ (i.e., subDLAs) that are more difficult to quantify in observations with high completeness.

The H I mass density associated with DLAs is captured in the first moment of $f(N_{\rm H\,I}, X)$, i.e.,

$$\rho_{\rm DLA}(X)\,dX = \frac{H_0 m_{\rm H}}{c}\int_{N_{\rm min}}^{\infty} N_{\rm H\,I} f(N_{\rm H\,I}, X)\,dN_{\rm H\,I}\,dX. \quad (4)$$

Obtaining Equation (4) required writing the mass density of H I in DLAs as

$$\rho_{\rm DLA} = n_{\rm DLA} m_{\rm DLA} \quad (5)$$

and

$$\rho_{\rm DLA}(X)\,dX = n_{\rm DLA}(X) A(X) m_{\rm H} N_{\rm H\,I}\,dX, \quad (6)$$

where $n_{\rm DLA}$ is the comoving number density of DLAs, $m_{\rm DLA}$ is the H I mass per DLA, $A(X)$ is the proper absorption cross section, and $m_{\rm H}$ is the mass of the hydrogen atom.

Upon inclusion of the critical density of the Universe ($\rho_{\rm crit,\,0}$), we obtain

$$\frac{\rho_{\rm DLA}(X)}{\rho_{\rm crit,\,0}}\,dX = \frac{H_0}{c}\frac{m_{\rm H}}{\rho_{\rm crit,\,0}}\int_{N_{\rm min}}^{\infty} N_{\rm H\,I} f(N_{\rm H\,I}, X)\,dN_{\rm H\,I}\,dX = \Omega_{\rm DLA}(X)\,dX. \quad (7)$$

Converting between $\rho_{\rm DLA}$ and $\rho_{\rm H\,I}$ requires knowledge of the shape of $f(N_{\rm H\,I}, X)$ toward lower $N_{\rm H\,I}$. For instance, observations of $f(N_{\rm H\,I}, X)$ at $z \sim 2$–4 (e.g., J. M. O'Meara et al. 2007; P. Noterdaeme et al. 2009; J. X. Prochaska et al. 2010; T. Zafar et al. 2013) have found that the contribution from subDLAs to $\rho_{\rm H\,I}$ is 10%–20%. For instance, N. H. M. Crighton et al. (2015) adopted a contribution from subDLAs of ≈17% at $z \sim 5$, corresponding to a correction factor

$$\rho_{\rm H\,I} = \delta_{\rm H\,I}\,\rho_{\rm DLA} = 1.2\,\rho_{\rm DLA}, \quad (8)$$

With studies showing no evidence of an evolution in $\delta_{\rm H\,I}$ across the $z \sim 2$–4 range (e.g., T. A. M. Berg et al. 2019), the choice of $\delta_{\rm H\,I} = 1.2$ is justified only up to $z \sim 4$. In this paper, we quantify $\delta_{\rm H\,I}$ directly from the subDLA sample (Section 4).

We can then write our final equation that quantifies $\rho_{\rm H\,I}$ from our observations as

$$\frac{\rho_{\rm HI}(X)}{\rho_{\rm crit,\,0}}\,dX = \frac{8\pi G}{3H_0}\frac{m_{\rm H}}{c}\delta_{\rm HI}\int_{N_{min}}^{\infty} N_{\rm HI} f(N_{\rm HI}, X)\,dN_{\rm HI}\,dX = \Omega_{\rm HI}(X)\,dX, \quad (9)$$

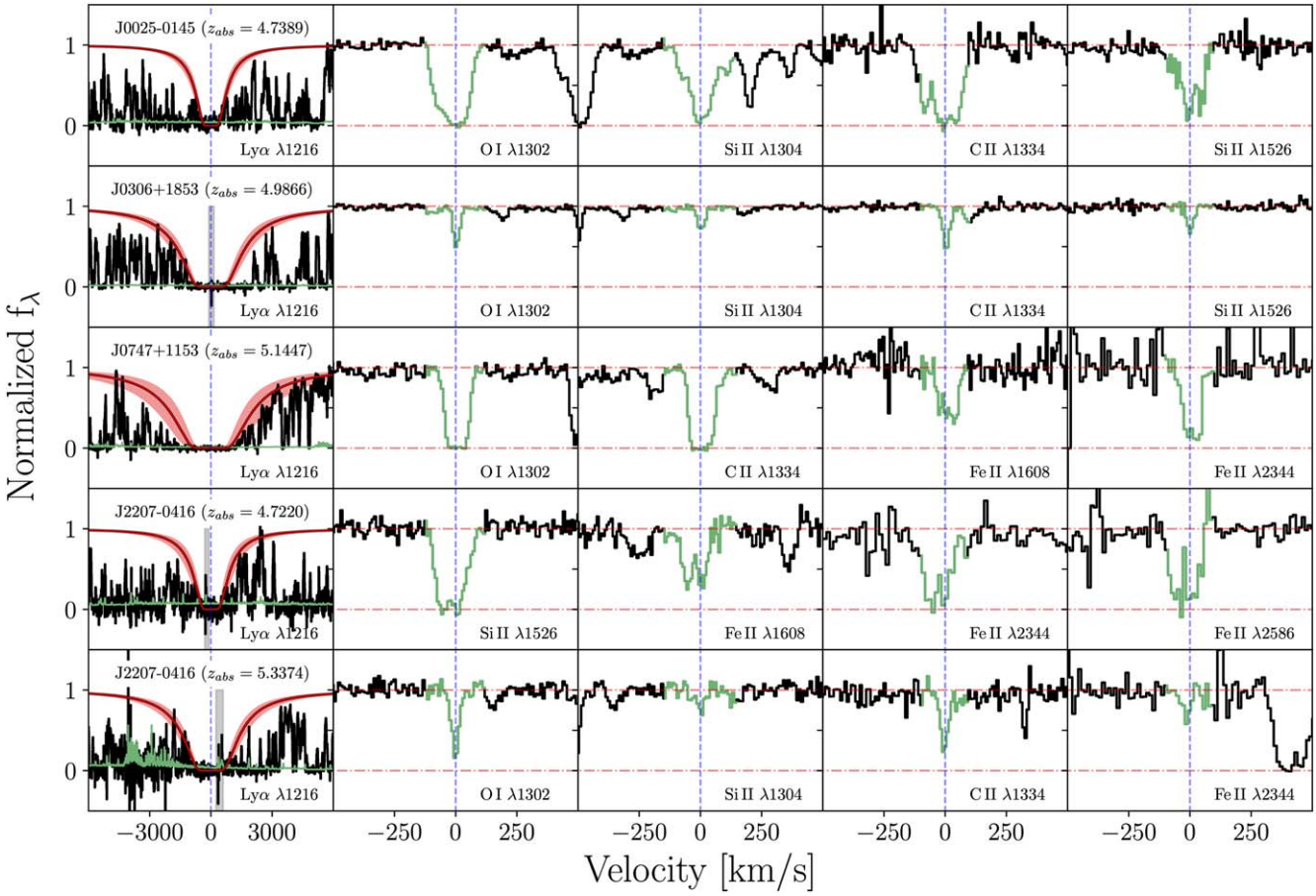

Figure 3. Detailed spectroscopic view of the five DLAs at $z \sim 5$ identified in Qz5. The rows show the five different DLAs. The leftmost column shows the QSO spectrum zoomed-in on the H I absorption of the DLA (black), the error on the flux (green), and the Voigt fit used to estimate $N_{\rm H\,I}$ (red). Residuals from sky subtraction are shaded in gray. The four rightmost columns show the continuum normalized QSO spectrum (black) zoomed-in on four different metal lines (green) that were used to determine the redshift of the H I gas absorber.

which was computed by discretely sampling the integrand in narrow $N_{\rm H\,I}$ bins ($dN_{\rm H\,I} = 10^{20}$ cm^{-2}) and integrating over redshift intervals.

We should also note that there is a distinction to be made between $\rho_{\rm H\,I}$ and the cosmic mass density of gas (often referred to as $\rho_{\rm gas}$). Previous work often determines $\rho_{\rm gas}$ by implementing a correction for the abundance of Helium, i.e.,

$$\rho_{\rm gas} = \delta_{\rm He}\ \rho_{\rm H\,I}. \tag{10}$$

A correction factor of $\delta_{\rm He} \approx 1.3$ is typically adopted (e.g., C. Péroux & J. C. Howk 2020; F. Walter et al. 2020).

4. Results

In Qz5, we detect five nonproximate DLAs at $z \sim 5$ (Table 2), which corresponds to <0.1 DLAs per sightline. This fraction is considerably lower than the ∼0.3 recovered by other surveys at $z \gtrsim 3.5$ (e.g., N. H. M. Crighton et al. 2015). This is quantitatively apparent in the DLA incidence rate, which has a value of $\ell_{\rm DLA}(X) = 0.034^{0.05}_{0.02}$ for Qz5 (see Table 3) and is plotted alongside estimates from other DLA studies in Figure 4. Here, the uncertainties on $\ell_{\rm DLA}(X)$ were estimated through Monte Carlo simulations where the number of DLAs detected is given by a Poisson distribution. We note that our $\ell_{\rm DLA}(X)$ is inconsistent at the $\sim 4.5\sigma$ level with the mean values from other surveys at $z \sim 4$–5.

Previous work has established that the identification of DLAs in low-resolution and low S/N spectra at $z \gtrsim 3.5$ is unreliable (P. Noterdaeme et al. 2012; M. Rafelski et al. 2012). For this reason, measurements in Figure 4 that are based on low-resolution, low S/N data beyond $z \gtrsim 3.5$ are excluded (P. Noterdaeme et al. 2009; J. X. Prochaska & A. M. Wolfe 2009; M.-F. Ho et al. 2020; R. Sánchez-Ramírez et al. 2016). As we will show in Section 5.1, these concerns also apply to low-resolution, high S/N data. Thus, the measurements by N. H. M. Crighton et al. (2015) at $z \sim 4$–5 are plotted as open square upper limits in Figure 4.

Considering only the most reliable values from the literature, Figure 4 suggests an evolution in the DLA incidence rate starting with $\ell_{\rm DLA}(X) \sim 0.03$ at $z \sim 5$ (this work), peaking around $\ell_{\rm DLA}(X) \sim 0.08$ at $z \sim 3$–4 (C. Péroux et al. 2003; J. X. Prochaska & A. M. Wolfe 2009; P. Noterdaeme et al. 2012; T. Zafar et al. 2013; R. Sánchez-Ramírez et al. 2016; M.-F. Ho et al. 2020), and then decreasing down to $\ell_{\rm DLA}(X) < 0.03$ at $z \sim 0$–1 (M. Neeleman et al. 2016; J. M. Shull et al. 2017).

Using the formalism described in Section 3.2, we also estimated $\rho_{\rm H\,I}$ at $z \sim 5$ as the addition between the H I mass densities of DLAs and subDLAs. We obtain $\rho_{\rm H\,I} = 0.56^{0.82}_{0.31} \times 10^8\ M_\odot$ Mpc^{-3} at $z \sim 5$ from Qz5, where the values from each component are reported in Table 3. For the uncertainties, we utilized Monte Carlo simulations that (1) bootstrap over the DLAs and subDLAs detected by Qz5

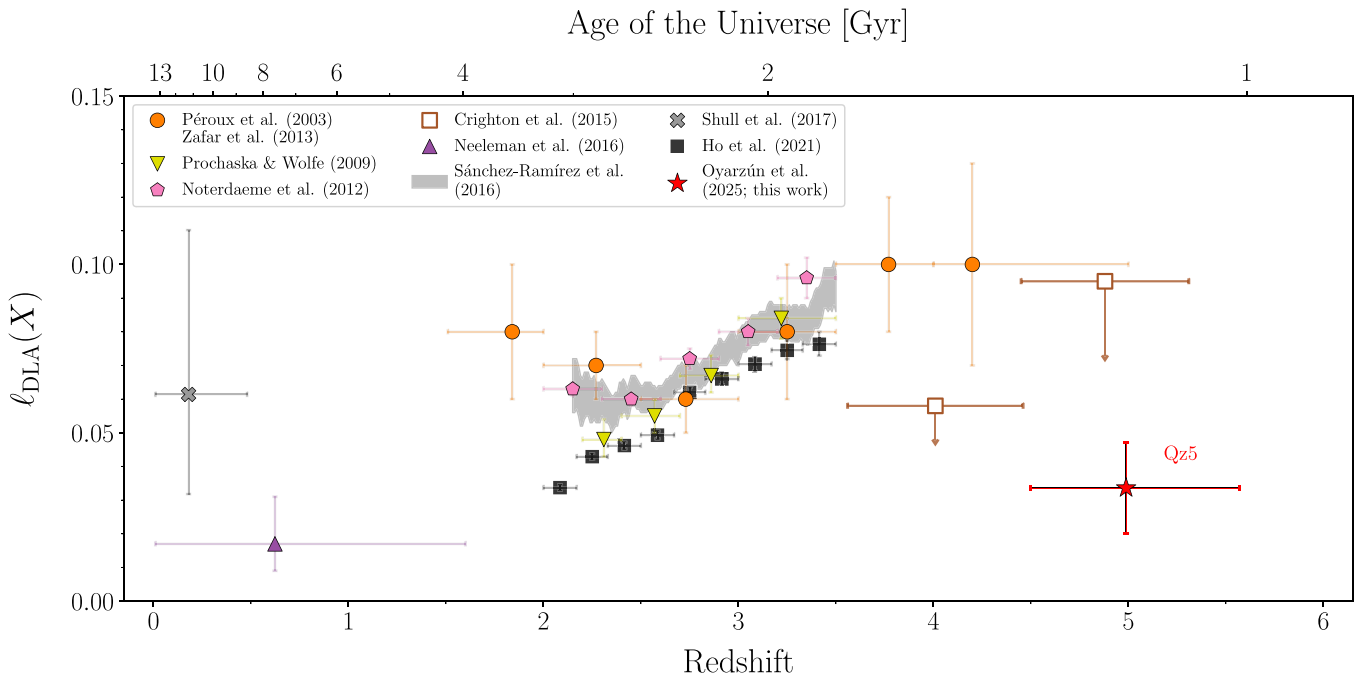

Figure 4. The DLA incidence rate at $z \sim 5$ derived with Qz5, along with estimates from other DLA surveys from the literature. Plotted are the measurements by C. Péroux et al. (2003) and T. Zafar et al. (2013, orange circles), J. X. Prochaska & A. M. Wolfe (2009, yellow triangles), P. Noterdaeme et al. (2012, pink pentagons), N. H. M. Crighton et al. (2015, brown squares), M. Neeleman et al. (2016, purple triangle), R. Sánchez-Ramírez et al. (2016, gray shading),), J. M. Shull et al. (2017, gray crosses), and M.-F. Ho et al. (2020, black squares). The measurements by N. H. M. Crighton et al. (2015) are shown as open square upper limits due to systematic biases (Section 5.1). Our data point at $z \sim 5$ (red star) is indicative of a much lower DLA incidence rate at $z \sim 5$ than at lower redshifts. We follow the convention that the error bar on the x-axis represents the width of the redshift bin encompassing the sample.

Table 3
Measurements of $\ell_{\rm DLA}(X)$ and $\rho_{\rm H\,I}$ at $z \sim 5$ with Different Subsamples and at Different Spectral Resolutions

Sample	$\ell_{\rm DLA}(X)$	$\rho_{\rm H\,I}$ ($10^8\,M_\odot\,{\rm Mpc}^{-3}$)
Qz5 subDLAs (uncorrected for line blending)	⋯	$0.174^{0.245}_{0.143}$
Qz5 subDLAs (corrected for ≈3% line blending; T. A. M. Berg et al. 2019)	⋯	$0.169^{0.238}_{0.139}$
Qz5 DLAs (ESI only)	0	0
Qz5 DLAs (X-SHOOTER only)	$0.048^{0.07}_{0.03}$	$0.57^{0.98}_{0.26}$
Qz5 DLAs (full sample)	$0.034^{0.05}_{0.02}$	$0.39^{0.68}_{0.18}$
Qz5 DLAs (after matching the resolution and S/N of N. H. M. Crighton et al. 2015)	$0.094^{0.12}_{0.067}$	$0.86^{1.37}_{0.53}$
N. H. M. Crighton et al. (2015) DLAs	$0.095^{0.12}_{0.07}$	$1.2^{1.44}_{0.99}$
N. H. M. Crighton et al. (2015)	$0.095^{0.12}_{0.07}$	$1.44^{1.73}_{1.19}$
Qz5 DLAs (full sample) + subDLAs (corrected)	$0.034^{0.05}_{0.02}$	$0.56^{0.82}_{0.31}$

Note. Columns show the survey (1), the DLA incidence rate (2), and the cosmic H I mass density at $z \sim 5$ (3).

according to a Poisson distribution and (2) assign the H I column densities from normal distributions with means $N_{\rm H\,I}$ and standard deviations $\Delta N_{\rm H\,I}$.

Our measurement is shown in Figure 5, along with other estimates from previous DLA campaigns. Because the value of $\rho_{\rm H\,I}$ is dependent on the value of H_0, only studies that report their choice of cosmological parameters are included in Figure 5 (C. Péroux et al. 2003; R. Guimarães et al. 2009; J. X. Prochaska & A. M. Wolfe 2009; P. Noterdaeme et al. 2009, 2012; A. Songaila & L. L. Cowie 2010; T. Zafar et al. 2013; N. H. M. Crighton et al. 2015; M. Neeleman et al. 2016; R. Sánchez-Ramírez et al. 2016; T. A. M. Berg et al. 2019). As we did for $\ell_{\rm DLA}(X)$, we excluded estimates of $\rho_{\rm H\,I}$ beyond $z \gtrsim 3.5$ that are based on low-resolution, low S/N data (i.e., P. Noterdaeme et al. 2009; J. X. Prochaska & A. M. Wolfe 2009; R. Sánchez-Ramírez et al. 2016). As in Figure 4, we also show estimates of $\rho_{\rm H\,I}$ obtained with low-resolution, high S/N data at $z \gtrsim 3.5$ as open square upper limits (N. H. M. Crighton et al. 2015). Also plotted in this figure are the fits to the data by C. Péroux & J. C. Howk (2020) and F. Walter et al. (2020) after decorrecting for the contribution from Helium ($\delta_{\rm He} = 1.3$).

All estimates that do not measure the subDLA contribution directly (including the fits by C. Péroux & J. C. Howk 2020 and F. Walter et al. 2020) were plotted assuming a correction factor of $\delta_{\rm H\,I} = 1.2$. This factor corresponds to a contribution to $\rho_{\rm H\,I}$ from low $N_{\rm H\,I}$ systems of ≈17% ($z \sim 2$–4; e.g., T. Zafar et al. 2013; T. A. M. Berg et al. 2019), which is considerably lower than the ≈30% that we measure with Qz5 (equivalent to $\delta_{\rm H\,I} = 1.44$). However, we note that our estimate of the H I mass density of subDLAs is not as precise as other measurements at $z \sim 2$–4 (T. Zafar et al. 2013; T. A. M. Berg et al. 2019) due to our smaller search path.

Despite the larger $\delta_{\rm H\,I}$ at $z \sim 5$, our measurement of $\rho_{\rm H\,I}$ is inconsistent with the $\rho_{\rm H\,I} \propto (1+z)^{0.57}$ fit obtained by C. Péroux & J. C. Howk (2020)—which captures the evolution of $\rho_{\rm H\,I}$ with redshift from most DLA surveys to date—at the 4σ level (in linear space; note that Figure 5 is in logarithmic space). These remarkably low values for $\rho_{\rm H\,I}$ from Qz5 are also recovered when the Keck/ESI and VLT/X-SHOOTER samples are treated separately and independently (see Table 3). Furthermore, adopting the lower value of $\delta_{\rm H\,I} = 1.2$ would only result in a lower $\rho_{\rm H\,I}$. We evaluate and discuss possible explanations for this deviation in Section 5.

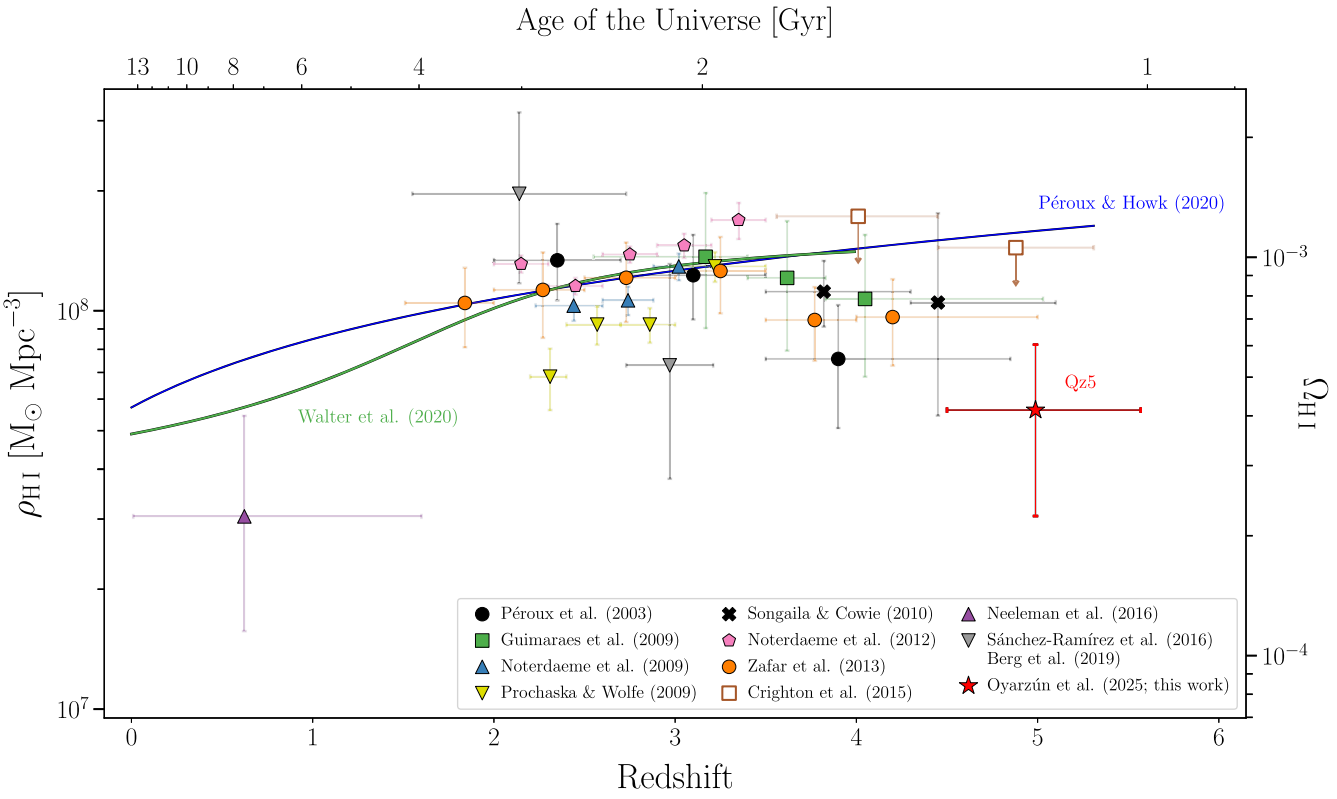

Figure 5. The cosmic H I mass density as a function of redshift as constrained by different DLA surveys. Included in this figure are the measurements by C. Péroux et al. (2003, black circles), R. Guimarães et al. (2009, green squares), P. Noterdaeme et al. (2009, blue triangles), J. X. Prochaska & A. M. Wolfe (2009, yellow triangles), A. Songaila & L. L. Cowie (2010, black crosses), P. Noterdaeme et al. (2012, pink pentagons), T. Zafar et al. (2013, orange circles), N. H. M. Crighton et al. (2015, brown squares), M. Neeleman et al. (2016, purple triangle), and R. Sánchez-Ramírez et al. (2016, gray triangles). Measurements at high redshift obtained with low spectral resolution data are shown as open symbol upper limits due to systematic biases (N. H. M. Crighton et al. 2015; Section 5.1). The blue line shows the fit by C. Péroux & J. C. Howk (2020) and the green line represents the fit by F. Walter et al. (2020). The Qz5 data point at $z \sim 5$ is plotted as a red star. The error bar on the x-axis represents the width of the redshift bin. All constraints and fits in this figure adopt a contribution from lower $N_{\rm H\,I}$ systems of $\delta_{\rm H\,I} = 1.2$, as found at $z \sim 2$–4. The only exception is Qz5, where we measure $\delta_{\rm H\,I} = 1.4$ (increasing our value for $\rho_{\rm H\,I}$ in comparison).

Figure 6 shows how $\rho_{\rm H\,I}$ varies with redshift after incorporating all techniques used for its estimation, with most measurements retrieved from the compilations by F. Walter et al. (2020) and C. Péroux & J. C. Howk (2020). The techniques plotted include 21 cm emission (M. A. Zwaan et al. 2005; R. Braun 2012; M. G. Jones et al. 2018), 21 cm emission stacking (P. Lah et al. 2007; J. Delhaize et al. 2013; J. Rhee et al. 2013; L. Hoppmann et al. 2015; N. Kanekar et al. 2016; A. Bera et al. 2019; A. Chowdhury et al. 2020), 21 cm absorption (K. Grasha et al. 2020), and Mg II absorption (S. M. Rao et al. 2017). DLAs are plotted as black pentagons, and we note that we excluded all low spectral resolution measurements beyond $z \gtrsim 3.5$ (P. Noterdaeme et al. 2009; J. X. Prochaska & A. M. Wolfe 2009; N. H. M. Crighton et al. 2015; R. Sánchez-Ramírez et al. 2016). All values plotted in Figures 5 and 6 are reported in Appendix C.

All together, the redshift evolution of $\rho_{\rm H\,I}$ is similar to that of $\ell_{\rm DLA}(X)$, with an increase from the highest measured redshifts until $z \sim 3$ and then steadily decreasing toward $z \sim 0$. The $\rho_{\rm H\,I} \propto (1+z)^{0.57}$ fit by C. Péroux & J. C. Howk (2020) accurately characterizes this trend at $z < 3$, but is in tension with our measurement at $z \sim 5$. Independently, some data points from studies at $z \sim 4$ also suggest a lower $\rho_{\rm H\,I}$ at $z > 3$ (C. Péroux et al. 2003; R. Guimarães et al. 2009; A. Songaila & L. L. Cowie 2010; T. Zafar et al. 2013). As we will show in Section 5.2, the data are better reproduced by models where $\rho_{\rm H\,I}(z)$ increases with cosmic time, peaks at $z \sim 3$, and then decreases at lower redshifts.

5. Discussion

Here, we discuss several possible interpretations for the low $\ell_{\rm DLA}(X)$ and $\rho_{\rm H\,I}$ at $z \sim 5$ recovered by Qz5. We start by quantifying the impact that survey design—primarily spectral resolution—has on the measured values for $\ell_{\rm DLA}(X)$ and $\rho_{\rm H\,I}$. We use this analysis to determine whether differences on the measured $\rho_{\rm H\,I}$ by different DLA surveys can be ascribed to systematic errors and/or statistical variations associated with the choice of sightlines. Then, we interpret the lower $\rho_{\rm H\,I}$ value at $z \sim 5$ within the context of our galaxy formation picture.

5.1. On the Measurements of $\rho_{\rm H\,I}$ at z $\sim$ 5 from DLA Surveys

Several DLA surveys have attempted to measure $\rho_{\rm H\,I}$ over the last two decades. Some of the earliest constraints (A. M. Wolfe et al. 1995)—and those that followed (e.g., J. X. Prochaska & A. M. Wolfe 2009) based on data from the SDSS Data Release 5 (J. K. Adelman-McCarthy et al. 2007)—are consistent with an increase in $\rho_{\rm H\,I}$ across the $z \sim 2$–4.5 range. However, the studies by M. Rafelski et al. (2012), P. Noterdaeme et al. (2012), and M. Neeleman et al. (2016) have pointed out that line blending in the Lyα forest can lead to issues in the identification of DLAs at relatively low spectral resolutions. For data from the SDSS, which features a

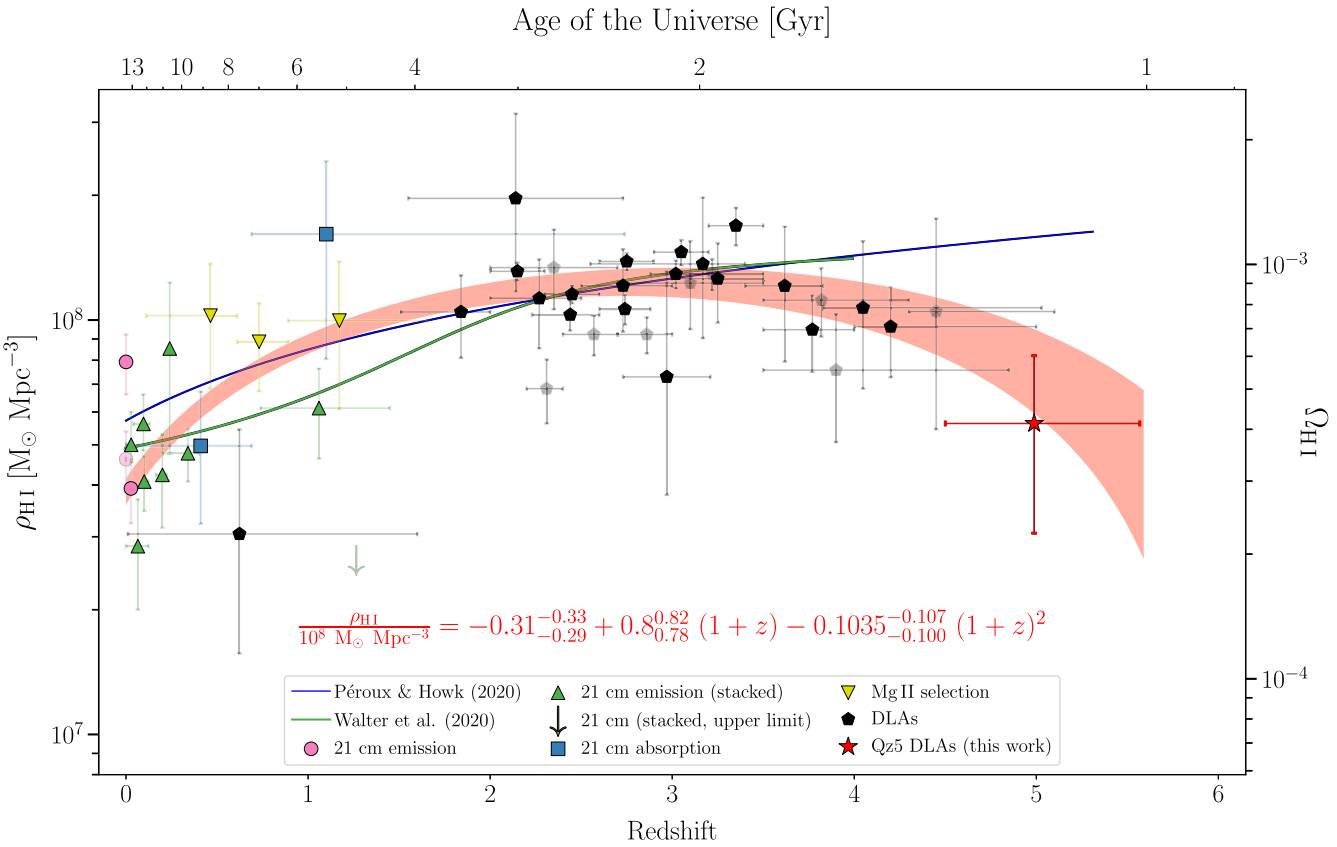

Figure 6. The cosmic H I mass density as a function of redshift according to different observational probes. Different symbols correspond to different techniques for constraining $\rho_{\rm H\,I}$. Constraints from 21 cm emission are plotted as pink circles and include the measurements by M. A. Zwaan et al. (2005), R. Braun (2012), and M. G. Jones et al. (2018). Results from 21 cm emission stacking are plotted as green upward-facing triangles and were originally obtained by P. Lah et al. (2007), J. Delhaize et al. (2013), J. Rhee et al. (2013), L. Hoppmann et al. (2015), A. Bera et al. (2019), and A. Chowdhury et al. (2020). The 21 cm emission stacking upper limit (downward pointing black arrow) was measured by N. Kanekar et al. (2016). The measurements of $\rho_{\rm H\,I}$ from 21 cm absorption plotted as blue squares correspond to the work by K. Grasha et al. (2020). The yellow downward-facing triangles show the constraints from S. M. Rao et al. (2017) using Mg II absorbers. The black pentagons show estimates from DLA statistics (see Figure 5) after excluding data points affected by resolution systematics (P. Noterdaeme et al. 2009; J. X. Prochaska & A. M. Wolfe 2009; N. H. M. Crighton et al. 2015; R. Sánchez-Ramírez et al. 2016). Our data point at $z \sim 5$ is plotted as a red star. Bayesian analysis reveals that the data in this figure are better reproduced by models with a peak in $\rho_{\rm H\,I}$ (red shading) instead of models where $\rho_{\rm H\,I}$ monotonically increases with redshift (e.g., C. Péroux & J. C. Howk 2020 or F. Walter et al. 2020). Due to statistical interdependence between some of the data, only the fully opaque data points were utilized for constraining the model posterior.

resolution of $R \sim 2000$, DLA identification is unreliable beyond $z \gtrsim 3.5$ (P. Noterdaeme et al. 2012). Further complicating the issue is spectral S/N, which for SDSS can be prohibitively low at these redshifts (S/N $\lesssim 3$). For these reasons, all DLA-based constraints on $\rho_{\rm H\,I}$ measured in SDSS data—including the BOSS of SDSS-III (BOSS; K. S. Dawson et al. 2013)—are highly uncertain (e.g., J. X. Prochaska & A. M. Wolfe 2009; S. Bird et al. 2017; M.-F. Ho et al. 2020).

The limitations of SDSS data at these redshifts motivated N. H. M. Crighton et al. (2015) to perform a dedicated search for DLAs at $z \sim 5$ at significantly higher S/N and slightly lower spectral resolution. We downloaded their data and measured a median S/N ~ 15 in the Lyα forest for their QSOs at $z > 4.5$ using the same approach that we adopted for Qz5 in Table 1, while their resolution is reported to be $R \sim 1300$ (G. Worseck et al. 2014). They deemed their measurement of the DLA incidence rate uncertain because it is strongly dependent on the number of DLAs with $N_{\rm H\,I} < 10^{20.5}\,{\rm cm}^{-2}$, which are challenging to accurately measure at low spectral resolutions. However, because $\rho_{\rm H\,I}$ is instead mostly driven by higher $N_{\rm H\,I}$ DLAs, they consider their estimate of $\rho_{\rm H\,I}$ to be more reliable. They recover a value of $\rho_{\rm H\,I} \approx 1.44 \times 10^8 M_\odot\,{\rm Mpc}^{-3}$, which is inconsistent with our measurement at the $\sim 4\sigma$ level.

The discrepancy in the value of $\rho_{\rm H\,I}$ at $z \sim 5$ between N. H. M. Crighton et al. (2015) and our work may be due to differences in either spectral resolution and/or statistical sampling. Note that while the S/N per pixel of S/N ~ 15 in N. H. M. Crighton et al. (2015) is higher than ours (Table 1), our S/N per Å is effectively higher by ≈30% if we account for the differences in spectral resolution and in spectral dispersion.

To study the impact of these effects on measurements of $\ell_{\rm DLA}(X)$ and $\rho_{\rm H\,I}$, we downgraded the spectral resolution, lowered the spectral dispersion, and added noise to the Qz5 data to match that of the survey by N. H. M. Crighton et al. (2015). We adopted $R \sim 1300$, a pixel size of 0.46 Å, and a median S/N per pixel of ∼15 in the Lyα forest, which are all representative of their final survey output (Giant Gemini GMOS survey; G. Worseck et al. 2014). Then, the reproduced data were subject to the same DLA detection and analysis methodology described in Section 3.1, with two exceptions. For consistency with the approach followed by N. H. M. Crighton et al. (2015), we excluded all metal line information and opted for a single QSO continuum fit. We note that the method

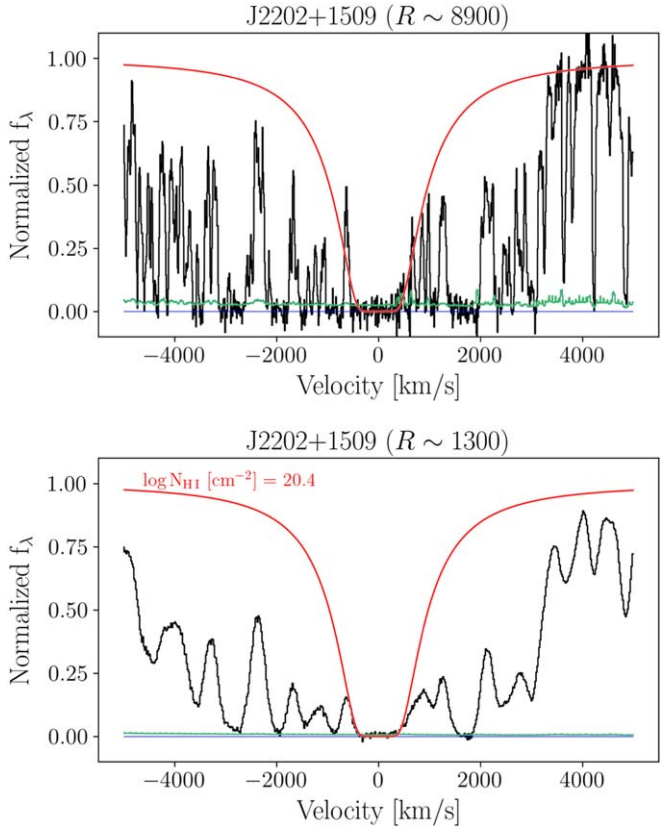

Figure 7. Example of how spectroscopy at low resolution can lead to false DLA detections at $z \gtrsim 3.5$. High-resolution data is shown on top and simulated, lower resolution data for the same system is shown at the bottom. The spectra are plotted in black, the errors in green, and the zero-level fluxes in blue. The high-column density DLA that is apparent in the low-resolution data ($N_{\rm H\,I} = 10^{20.4}\,{\rm cm}^{-2}$; red) is inconsistent with the high-resolution spectrum. Misidentifications of this kind can lead to overestimated values for $\rho_{\rm H\,I}$ at $z \gtrsim 3.5$ (see Table 3).

to search for DLAs adopted by N. H. M. Crighton et al. (2015) was visual inspection, in similar fashion to our work.

We found a total of 14 DLAs in the downgraded spectra, which corresponds to almost three times the number of DLAs detected in the original, high-resolution data set (see Figure 7 for an example). At first glance, this spurious DLA rate (9/14 ≈ 64%) is at odds with the ≲15%–30% rate estimated by N. H. M. Crighton et al. (2015) on high-resolution and/or in mock spectra. However, we should note that N. H. M. Crighton et al. (2015) estimate that this number can reach ≈55% at $N_{\rm H\,I} \sim 10^{20.3}$–$10^{20.6}\,{\rm cm}^{-2}$, which is exactly the same $N_{\rm H\,I}$ regime in which we found most of the spurious DLAs.

We should note that we detected almost all originally identified DLAs (4/5) in the downgraded, low-resolution spectra. This result is not in disagreement with N. H. M. Crighton et al. (2015), who determined that ∼80%–90% of DLAs are recovered at lower resolutions. Although differences between the log $N_{\rm H\,I}$ measured in the low and high-resolution data sets can be significant (0.2 dex), we do not identify any systematic biases in the ability to recover the $N_{\rm H\,I}$ of real DLAs accurately. This was also the conclusion reached by N. H. M. Crighton et al. (2015) from their simulations.

Our measurements from the downgraded data were used to estimate a low-resolution counterpart of $\rho_{\rm H\,I}$ from our survey, and the outcome is reported in Table 3. Comparison reveals that estimates of $\ell_{\rm DLA}(X)$ and $\rho_{\rm H\,I}$ from the downgraded Qz5 and the survey by N. H. M. Crighton et al. (2015) are consistent within the uncertainties. We note that we are able to replicate their measurements both before and after they implement multiplicative resolution correction factors (since they are small; ≲10%). As apparent in Table 3, our analysis suggests that resolution correction factors are much larger (∼100% for $\rho_{\rm H\,I}$).

It is evident from the procedures described above that lower spectral resolutions can lead to systematically higher recovered values for both $\ell_{\rm DLA}(X)$ and $\rho_{\rm H\,I}$. For this reason, the N. H. M. Crighton et al. (2015) data point at $z \sim 5$ in Figures 5 and 6 is plotted as an upper limit and will not be considered in the analysis that follows in Section 5.2.

5.2. Statistical Significance of the Low $\rho_{H\,I}$ at z $\gtrsim$ 3.5

As apparent from the error bars in Figures 4 and 5, our measurements of both $\ell_{\rm DLA}(X)$ and $\rho_{\rm H\,I}$ are not particularly precise. The uncertainties on $\ell_{\rm DLA}(X)$ and $\rho_{\rm H\,I}$ are dominated by the limited search path of Qz5, which features only 63 sightlines. This is because attaining large search paths at $z > 3$ is difficult, since faint QSOs at these redshifts require massive programs at large telescopes. This can be appreciated in how the typical uncertainties on $\ell_{\rm DLA}(X)$ and $\rho_{\rm H\,I}$ in the literature increase toward $z > 3$ in Figures 4 and 5.

Even so, other results from the literature suggest that low values for $\rho_{\rm H\,I}$ are not driven by the particular sightlines comprising Qz5. First, we have shown that the survey by N. H. M. Crighton et al. (2015), which features a lower search path than ours at $z > 5$, is affected by resolution issues, and thus their value for $\rho_{\rm H\,I}$ at $z \sim 5$ is uncertain and likely overestimated. Second, the measurements of $\rho_{\rm H\,I}$ at $z > 3$ by R. Guimarães et al. (2009), C. Péroux et al. (2003), A. Songaila & L. L. Cowie (2010), and T. Zafar et al. (2013) are consistent with a decrease in $\rho_{\rm H\,I}$ with redshift (see Figure 5). To quantify this, we can compare two different $\rho_{\rm H\,I}$ models: one that is flat/increasing with redshift (Model $\mathcal{A}$) and another where $\rho_{\rm H\,I}$ is allowed to increase, peak, and then decrease with redshift (Model $\mathcal{B}$). We can make Model $\mathcal{A}$ match the parameterization suggested by C. Péroux & J. C. Howk (2020), which has the functional form

$$\frac{\rho^{\mathcal{A}}_{\rm H\,I}(z)}{10^8\,M_\odot\,{\rm Mpc}^{-3}} = a\,(1+z)^{\gamma}. \tag{11}$$

For the second model, we considered the parameterization

$$\frac{\rho^{\mathcal{B}}_{\rm H\,I}(z)}{10^8\,M_\odot\,{\rm Mpc}^{-3}} = c_0 + c_1\,(1+z) + c_2\,(1+z)^2. \tag{12}$$

Both models were fitted to the data in Figure 6 after careful assessment of redundant, correlated data points. We included the 21 cm emission measurements by P. Lah et al. (2007), R. Braun (2012), J. Delhaize et al. (2013), J. Rhee et al. (2013), L. Hoppmann et al. (2015), M. G. Jones et al. (2018), A. Bera et al. (2019) and A. Chowdhury et al. (2020), while the constraints by M. A. Zwaan et al. (2005) and N. Kanekar et al. (2016) where excluded due to their respective redundancy with the measurements by J. Delhaize et al. (2013) and A. Chowdhury et al. (2020). The estimates from 21 cm absorption (K. Grasha et al. 2020) and from Mg II selected absorbers (S. M. Rao et al. 2017) were also included. Finally, we utilized the data points from the DLA surveys by R. Guimarães et al. (2009), P. Noterdaeme et al. (2012), T. Zafar et al. (2013),

M. Neeleman et al. (2016), R. Sánchez-Ramírez et al. (2016), and Qz5. Because of the inclusion of the study with SDSS by P. Noterdaeme et al. (2012), we excluded the measurements by P. Noterdaeme et al. (2009) and J. X. Prochaska & A. M. Wolfe (2009). Similarly, because of the inclusion of the work by T. Zafar et al. (2013), we removed the constraints by C. Péroux et al. (2003) and A. Songaila & L. L. Cowie (2010).

We decided to use a Bayesian approach to constrain the posterior distributions of these models. We adopted flat, bounded priors for all parameters, and we fitted for asymmetric errors in the $\rho_{\rm H\,I}$ estimates. The posteriors were quantified in multidimensional grids for all model parameters.

To determine what model best reproduces the data, we can turn to the Bayes factor. This quantity is defined as

$$B_{\mathcal{AB}} = p_{\mathcal{A}}/p_{\mathcal{B}}, \tag{13}$$

where $p_{\mathcal{A}}$ and $p_{\mathcal{B}}$ correspond to the marginal likelihoods of models $\mathcal{A}$ and $\mathcal{B}$, respectively. Note that the use of the marginal likelihoods makes the Bayes factor ideal for comparing models with different number of parameters (i.e., Model $\mathcal{B}$ is penalized for having one more free parameter than Model $\mathcal{A}$). We obtain a value of

$$\log B_{\mathcal{AB}} < -5, \tag{14}$$

which according to Jeffrey's scale corresponds to decisive evidence in favor of Model $\mathcal{B}$. Thus, we conclude that literature measurements of $\rho_{\rm H\,I}$ are most consistent with a model that allows for $\rho_{\rm H\,I}(z)$ to increase with cosmic time, peak, and then decrease toward low redshift.

We found the best-fit parameters of Model $\mathcal{B}$ to be

$$c_0 = -0.31 \pm 0.02, \tag{15}$$

$$c_1 = 0.8 \pm 0.02, \text{and} \tag{16}$$

$$c_2 = -0.1035 \pm 0.0035. \tag{17}$$

The solution achieved with these parameters is plotted in Figure 6.

5.3. Interpretation for the Low $\rho_{H\,I}$ at z $\gtrsim$ 3.5

We have concluded that observations show evidence for an increase in $\rho_{\rm H\,I}$ from $z \sim 5$ to $z \sim 3$. To interpret this trend, we can turn to analytic arguments for the evolution of the baryonic components of galaxies with cosmic time (e.g., F. Walter et al. 2020). In particular, we are interested in the mechanisms that dictate the assembly of H I gas in galaxies.

The baryonic budget of galaxies is formed and replenished through the accretion (and cooling) of neutral and ionized gas from the cosmic web (e.g., N. Bouché et al. 2010; L. J. Tacconi et al. 2018). Thus, the rate at which the baryonic budgets of galaxies grow with cosmic time is tied to the rate at which halos accrete matter. Taking the halo mass accretion rate in ΛCDM (A. Rodríguez-Puebla et al. 2016) and a baryonic matter fraction that is constant with redshift yields baryonic mass densities inside galaxies ($\rho_{\rm b,gal}$) that increase monotonically with cosmic time (F. Walter et al. 2020). This behavior is a direct result of how the halo mass function grows as the Universe evolves.

Some theoretical models prescribe an evolution with redshift for $\rho_{\rm H\,I}$ that is very similar to that of $\rho_{\rm b,gal}$. In these prescriptions, the increase of $\rho_{\rm H\,I}$ with time naturally follows accretion of matter from the cosmic web. In a two step-process, this accretion of gas is turned into stars through (1) the infall of neutral and ionized onto extended H I gas reservoirs through cold mode accretion and (2) the cooling of this gas that leads to the production of H_2 and the formation of stars (e.g., F. Walter et al. 2020). Therefore, the increase in $\rho_{\rm H\,I}$ with cosmic time is followed by an increase in the cosmic molecular gas mass density ($\rho_{\rm H_2}$) and an increase in the cosmic star formation rate density (ψ_*).

It stands to reason that the normalization of $\rho_{\rm H\,I}(z)$ is also directly linked to how and when H I mass builds up in galaxies. For instance, G. Popping et al. (2014) and M. Berry et al. (2014, 2016)—who utilized the semianalytic models developed by R. S. Somerville & J. R. Primack (1999) and R. S. Somerville et al. (2008, 2012) to study the evolution of $\rho_{\rm H\,I}$ with cosmic time—predict $\rho_{\rm H\,I}$ to increase with time before turning over and decreasing toward $z < 1$ (see Figure 8). Similar trends were found in the GALFORM (C. D. P. Lagos et al. 2014), GAEA (M. Spinelli et al. 2020), and T. Theuns (2021) semianalytic models, as well as in the L-GALAXIES simulation (H. Martindale et al. 2017; B. M. B. Henriques et al. 2020). On the other hand, the build-up of H I occurs mostly at $z > 4$ in other studies (Figure 8). In the EAGLE simulation (A. Rahmati et al. 2015), $\rho_{\rm H\,I}$ only starts to show evidence of an initial increase toward $z \gtrsim 3.5$. In IllustrisTNG (M. Vogelsberger et al. 2014) and in ColdSim (U. Maio et al. 2022), $\rho_{\rm H\,I}$ builds up before $z \sim 5$. Here, the IllustrisTNG constraint corresponds to the average between the measurements by F. Villaescusa-Navarro et al. (2018) and G. Popping et al. (2019; as reported in Figure 3 of R. M. Yates et al. 2021). Our analysis of the observational data reveals that this build-up is still ongoing at $z \sim 5$ and continues out to at least $z \sim 4$.

As pointed out by R. M. Yates et al. (2021), differences in the amount and/or the column density of H I gas in the CGM of galaxies between theoretical work can sometimes exceed $\gtrsim$50%. Thus, the presence (or lack thereof) of high-column density H I gas far out into the IGM and/or the CGM of galaxies (beyond 2 effective radii; C. Byrohl et al. 2021; R. M. Yates et al. 2021) also emerges as an important factor in determining the normalization of $\rho_{\rm H\,I}$. By extension, variations in the amount of H I in the CGM of galaxies with cosmic time could also impact the evolution of $\rho_{\rm H\,I}(z)$.

Evidence suggests that $\rho_{\rm H\,I}$ (as derived by DLA surveys) is indeed sensitive to the amount of H I gas in the CGM. First, DLAs typically contain little H_2 (based on the lack of Lyman–Werner absorption; e.g., R. A. Jorgenson & A. M. Wolfe 2014), hinting that DLAs rarely trace gas near star-forming regions (as predicted by simulations; e.g., J. Stern et al. 2021; J. Stern et al. 2024). Second, the projected separations between DLAs and associated galaxies can exceed 40 kpc at $z \sim$ 2–4, which is indicative of CGM scales (e.g., M. Fumagalli et al. 2017; J. K. Krogager et al. 2017; M. Neeleman et al. 2017; M. Neeleman et al. 2018, 2019; R. Mackenzie et al. 2019; J. X. Prochaska et al. 2019; N. Kanekar et al. 2020; N. H. P. Rhodin et al. 2021; B. Kaur et al. 2021, 2022a, 2022b; E. K. Lofthouse et al. 2023; G. A. Oyarzún et al. 2024; see also L. Christensen et al. 2014; A. Hamanowicz et al. 2020). This is consistent with the declining incidence rate of Mg II absorbers toward $z > 2$ (M. S. Matejek & R. A. Simcoe 2012), under the assumption that these Mg II trace the population of DLAs at these redshifts (e.g., T. A. M. Berg et al. 2017; S. M. Rao et al. 2017). As samples of H I-selected galaxies continue to grow, it will be interesting to establish if any evolution with redshift is observed in the projected separations between galaxies and DLAs.

In this framework that envisions $\rho_{\rm H\,I}$ evolving with $\rho_{\rm b,gal}$, one would not expect that $\rho_{\rm H\,I}$ before the formation of the first stars

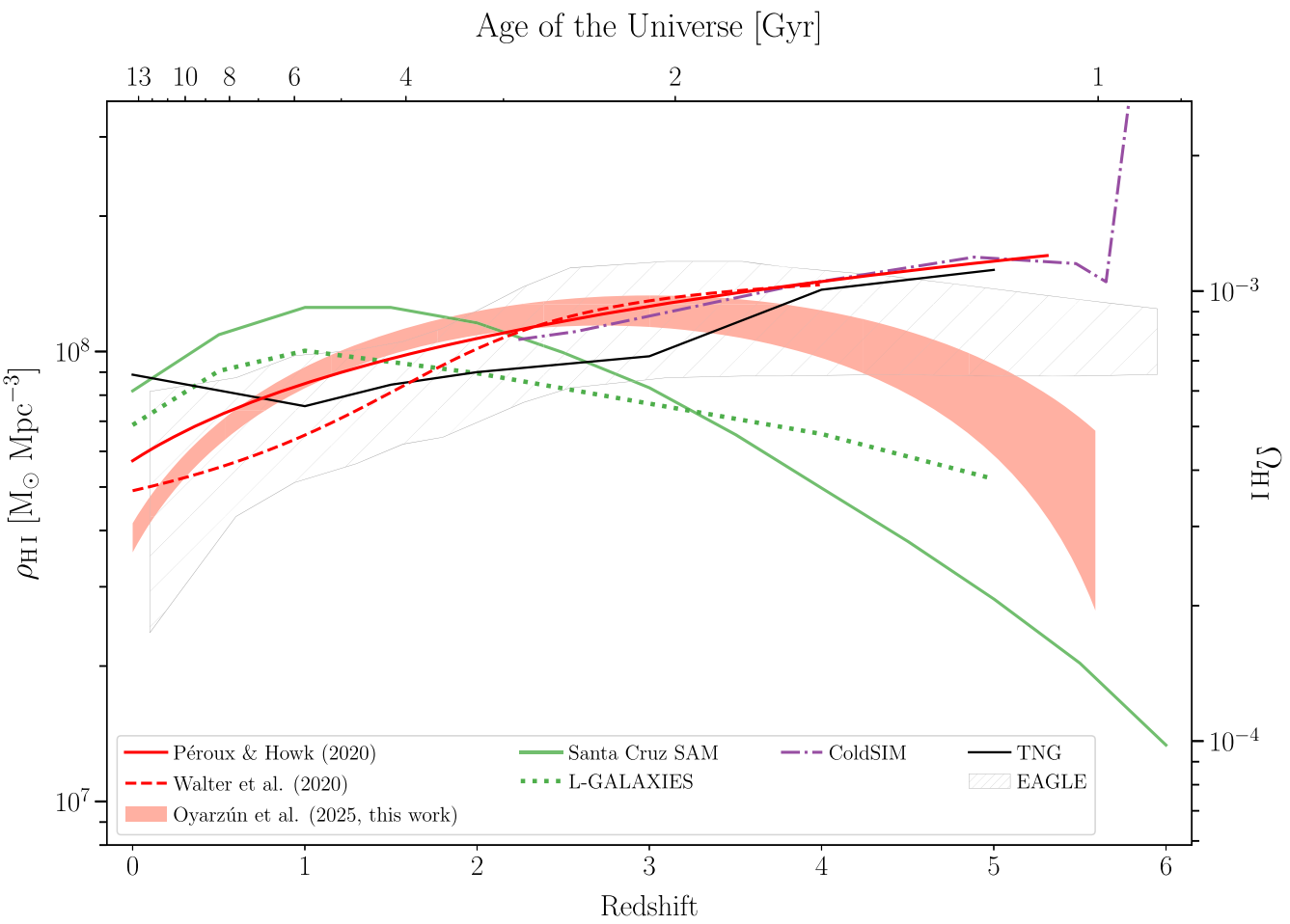

Figure 8. The cosmic H I mass density as a function of redshift. Plotted are constraints from the data (C. Péroux & J. C. Howk 2020; F. Walter et al. 2020 and this work), semianalytic models (Santa Cruz and L-GALAXIES; G. Popping et al. 2014; B. M. B. Henriques et al. 2020), hydrodynamical simulations with an explicit H I component (ColdSim; U. Maio et al. 2022), and hydrodynamical simulations without built-in partitioning of the different hydrogen components (IllustrisTNG and EAGLE; M. Vogelsberger et al. 2014; A. Rahmati et al. 2015).

corresponds to the cosmic mass density of baryonic matter. As redshift increases, we expect the fraction of $\rho_{\rm H\,I}$ that is present in low $N_{\rm H\,I}$ gas in the IGM to increase, driving constraints on $\rho_{\rm H\,I}$—as measured by probes of high-$N_{\rm H\,I}$ gas—apart from the true value of $\rho_{\rm H\,I}$. We identify tentative evidence that this distinction becomes relevant at high redshift in the major contribution of subDLAs to $\rho_{\rm H\,I}$. While we know that subDLAs probe 10%–20% of the H I gas mass in the Universe at $z \sim 2$–4 (e.g., T. Zafar et al. 2013; T. A. M. Berg et al. 2019), we recover a higher value of ≈30% at $z \sim 5$ with Qz5 (albeit with limited statistical power). In summary, and as also pointed out by K. E. Heintz et al. (2022), there is a distinction to be made between $\rho_{\rm H\,I}$ (as probed by gas in the ISM and CGM of galaxies) and true $\rho_{\rm H\,I}$ (which also accounts for gas in the IGM), especially at very high redshift.

5.4. Alternative Scenarios for the Low $\rho_{H\,I}$ at z $\gtrsim$ 3.5

An alternative scenario for the lower value of $\rho_{\rm H\,I}$ at $z \gtrsim 3.5$ may emerge from recent studies of the Lyα and Lyβ forests, where fluctuations in the neutral gas fraction down to $z \sim 5$–6 have been identified (G. D. Becker et al. 2015; S. E. I. Bosman et al. 2018, 2022; Y. Qin et al. 2021; A. Grazian et al. 2023; Y. Zhu et al. 2023, 2024; B. Spina et al. 2024). In this context, one may consider that the end of the reionzation of the Universe is somehow connected with the changes in $\rho_{\rm H\,I}$ that we observe. Evidence suggests that a direct connection is unlikely, with recent studies revealing that high-$N_{\rm H\,I}$ gas can form well before the end of reionization (DLAs at $z \sim 10$; K. E. Heintz et al. 2024). Thus, our current understanding is that the formation of high-column density H I gas and the reionization of the IGM are not necessarily coupled and that they can occur at widely different redshifts.

It is also worth discussing whether the turnover in $\rho_{\rm H\,I}$ at $z \gtrsim 3.5$ could be driven by redshift variations in the sensitivity of absorption studies to high-$N_{\rm H\,I}$ gas. Dust extinction stands out as a the primary candidate for this potential bias, with studies dating back more than three decades showing that QSO sightlines containing DLAs feature higher dust reddening than QSO sightlines lacking in DLAs (S. M. Fall et al. 1989, 1996; Y. C. Pei et al. 1991, 1999; S. M. Fall & Y. C. Pei 1993; Y. C. Pei & S. M. Fall 1995). That said, studies with SDSS and DESI have revealed that this effect is minor, at least out to $z \sim 4$ (M. T. Murphy & M. L. Bernet 2016; L. Napolitano et al. 2024). If this effect was to become more significant toward $z \gtrsim 4$, it could contribute to and/or fabricate the turnover in $\rho_{\rm H\,I}$ that we report in this paper.

6. Summary

We have conducted Qz5, a spectroscopic survey of 63 bright QSOs at $z \sim 4.7$–5.7 with Keck/ESI and VLT/X-SHOOTER that is aimed at constraining $\ell_{\rm DLA}(X)$ and $\rho_{\rm H\,I}$ at $z \sim 5$. Qz5

stands out because of the high resolution ($R \sim 7000$–9000) of the spectra, enabling us to constrain $\ell_{\rm DLA}(X)$ and $\rho_{\rm H\,I}$ with accuracy by minimizing biases that that can affect studies at low spectral resolutions. We found a total of five nonproximate DLAs in the 63 QSOs, which translates into a DLA incidence rate of $\ell_{\rm DLA}(X) \sim 0.034^{0.05}_{0.02}$. We estimate that the contribution of subDLAs toward $\rho_{\rm H\,I}$ is higher at $z \sim 5$ (≈30%) than at lower redshifts (≈ 17%). Accounting for the contribution of both DLAs and subDLAs, we measure a value for the cosmic H I mass density at $z \sim 5$ of $\rho_{\rm H\,I} = 0.56^{0.82}_{0.31} \times 10^8\,M_\odot\ {\rm Mpc}^{-3}$. These values for $\ell_{\rm DLA}(X)$ and $\rho_{\rm H\,I}$ are ∼2–4σ lower than previously reported values at $z \sim 2$–5.

To understand the discrepancy between our measurements and the results from previous work, we studied the impact of spectral resolution on estimates of $\ell_{\rm DLA}(X)$ and $\rho_{\rm H\,I}$. We focused on replicating the observational setup by N. H. M. Crighton et al. (2015), which stands out as a high S/N study of $\rho_{\rm H\,I}$ at $z \sim 5$ from DLAs (S/N ∼ 15, $R \sim 1300$). We show that lowering the resolution of our survey—from $R \gtrsim 7000$ to $R \sim 1300$—leads to systematically higher estimates of $\ell_{\rm DLA}(X)$ and $\rho_{\rm H\,I}$, accounting for any discrepancies. We therefore conclude that high-resolution spectroscopy is critical for accurately measuring $\ell_{\rm DLA}(X)$ and $\rho_{\rm H\,I}$ toward $z \gtrsim 3.5$.

Our measurements at $z \sim 5$ indicate that $\ell_{\rm DLA}(X)$ and $\rho_{\rm H\,I}$ at $z \sim 5$ are lower than the widely adopted fit to the observational data by C. Péroux & J. C. Howk (2020) with 4σ significance. After the exclusion of biased constraints at $z > 3.5$ and the inclusion of our new measurement at $z \sim 5$, the preference for a $\rho_{\rm H\,I} = \rho_{\rm H\,I}(z)$ model that peaks at $z \sim 3$ is decisive, according to a Bayesian comparison. This means that observations of $\rho_{\rm H\,I}(z)$ from DLAs are best reproduced by models that increase with cosmic time, peak at $z \sim 3$, and then decrease at low redshift.

In conclusion, we show for the first time that $\rho_{\rm H\,I}$ follows a similar evolutionary shape as the ψ_* and $\rho_{\rm H_2}$, corresponding to a rise at early times from the inflow of gas from the cosmic web onto the halos of galaxies. This behavior is then followed by a peak at $z \sim 3$ and a turnover at $z < 2$. To constrain the highly uncertain peak of $\rho_{\rm H\,I}$ in cosmic time, additional high-resolution, high S/N surveys of QSOs at $z = 3$–5.5 are needed. Regardless, it appears that $\rho_{\rm H\,I}$ peaks earlier than the ψ_* and $\rho_{\rm H_2}$, which already constrains galaxy formation models.

Acknowledgments

We are thankful to the reviewer of this manuscript for the constructive comments and suggestions. The authors would also like to acknowledge Nissim Kanekar for the valuable conversations and insightful comments in regards to this manuscript. This material is based upon work supported by the National Science Foundation under grant No. 2107989. M.R. also acknowledges support from the STScI's Director's Discretionary Research Funding (grant ID D0101.90228). L. C. is supported by DFF/Independent Research Fund Denmark, grant ID 2032-00071. S.L. acknowledges support by FONDECYT grant 1231187. This work made use of Astropy,[20] a community-developed core Python package and an ecosystem of tools and resources for astronomy (Astropy Collaboration et al. 2013, 2018, 2022). This work also made use of `linetools` (J. X. Prochaska et al. 2016).

Appendix A
Qz5 Spectra

The data for the Qz5 survey is available for download at DOI: 10.5281/zenodo.14825981 and http://www.rafelski.com/data/DLA/qz5/. The spectra are shown in Figures 9 through 12.

[20] http://www.astropy.org

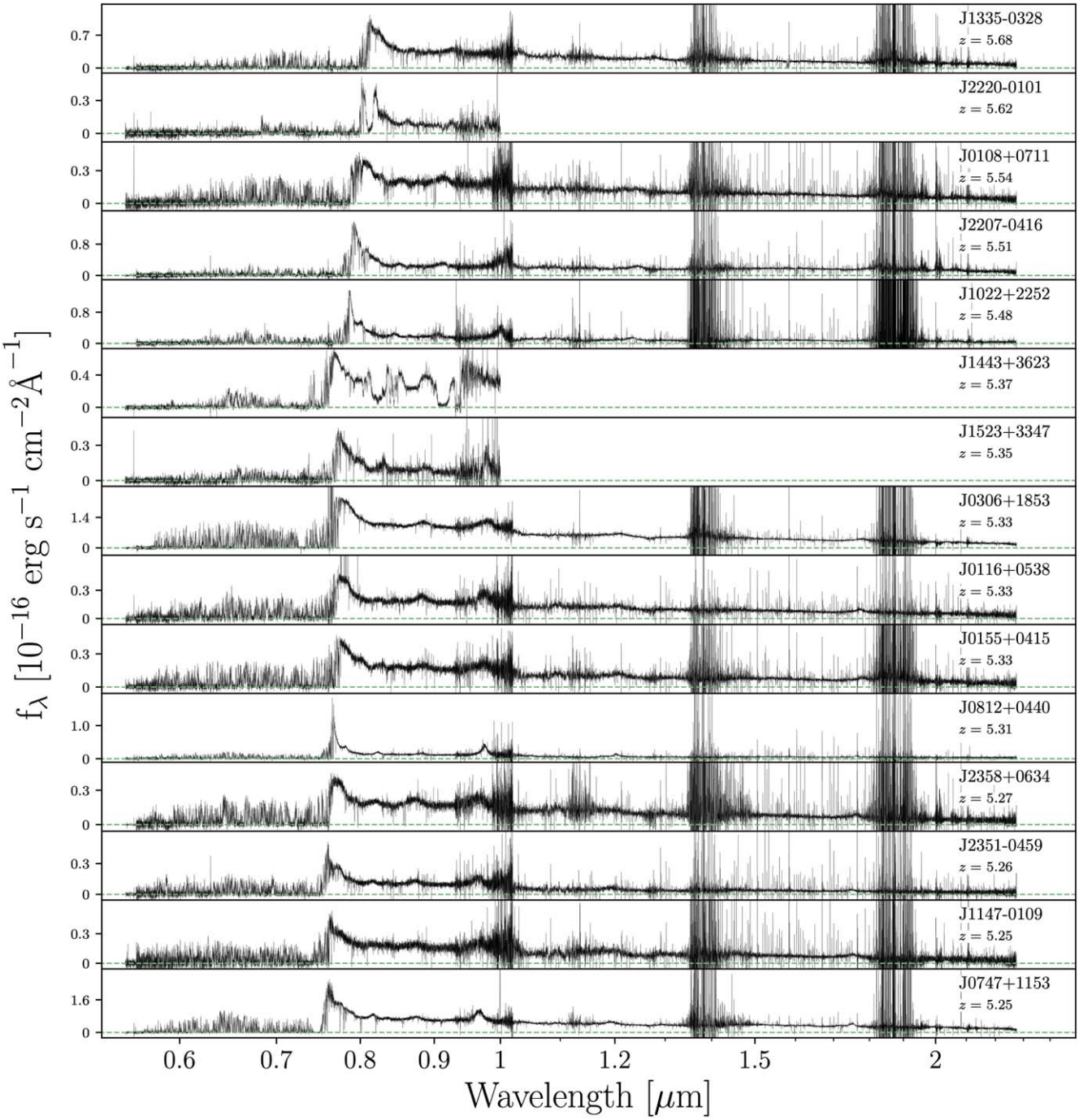

Figure 9. The QSO spectra utilized in this study.

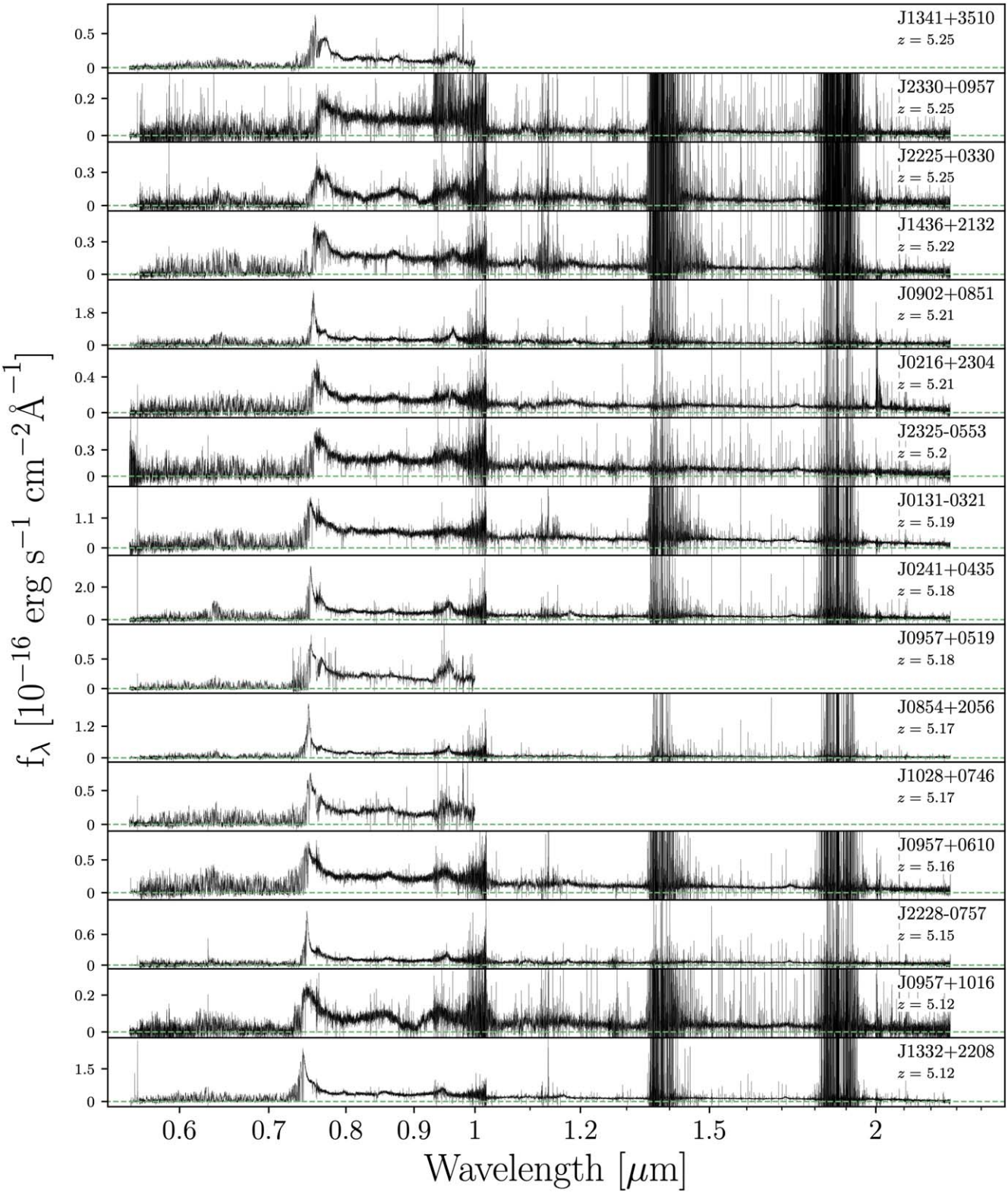

Figure 10. The QSO spectra utilized in this study.

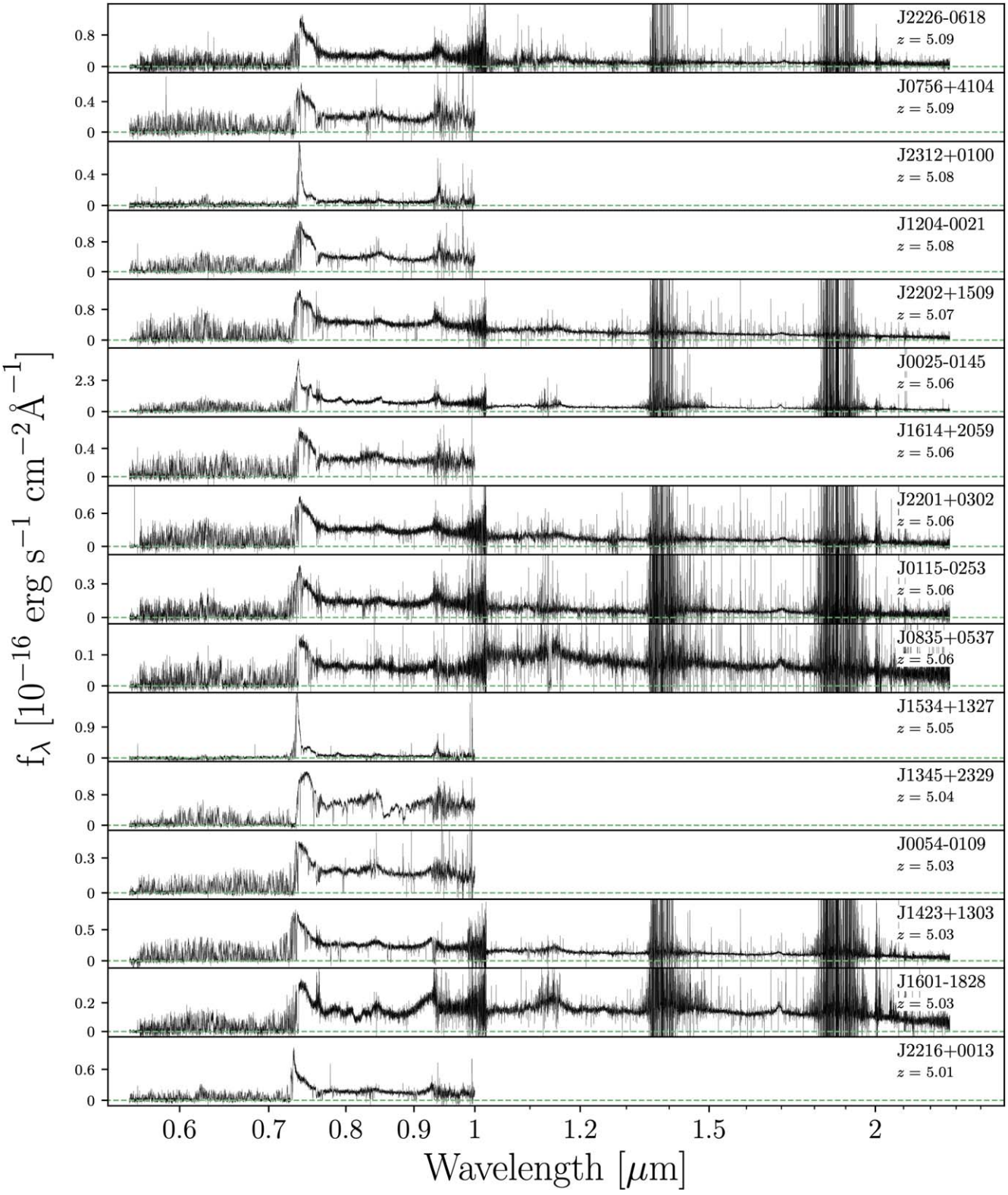

Figure 11. The QSO spectra utilized in this study.

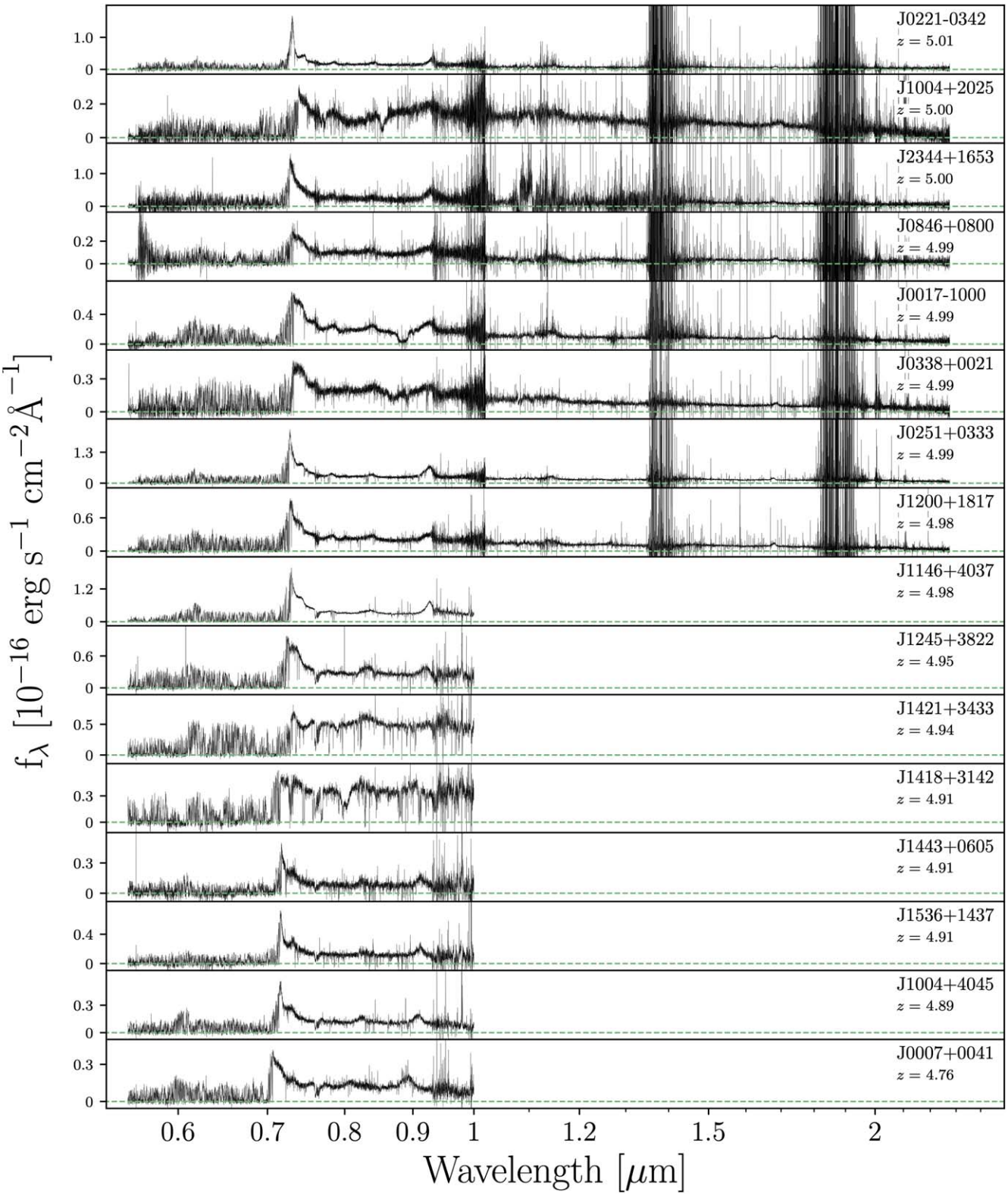

Figure 12. The QSO spectra utilized in this study.

Appendix B
H I Absorbers Identified in the Spectra

We outline in Table 4 all H I absorbers that were identified as DLA candidates during our search outlined in Section 3.1. The absorbers are grouped by QSO sightline and ordered according to the absorption redshift. The notes column specifies the reason for the inclusion or exclusion of the absorber into our analysis of $\ell_{\rm DLA}(X)$ and $\rho_{\rm H\,I}$.

Table 4
H I Absorbers Identified in Qz5

QSO	R.A.	Decl.	z_{em}	z_{abs}	Notes	$\log N_{\rm H\,I}$ ($\rm cm^{-2}$)
J0007+0041	00:07:49.17	00:41:19.62	4.76	4.7330	N: Proximate DLA	20.6 ± 0.3
J0025-0145	00:25:26.84	-01:45:32.50	5.06	4.7389	Y: DLA	20.3 ± 0.15
J0116+0538	01:16:14.31	05:38:17.59	5.33	5.108	Y: subDLA	19 ± 0.2
...	...	...	...	5.113	Y: subDLA	19.3 ± 0.2
J0131-0321	01:31:27.35	-03:21:00.08	5.19	4.654	Y: subDLA	19.0 ± 0.2
...	...	...	...	4.962	Y: subDLA	19.5 ± 0.2
J0306+1853	03:06:42.51	18:53:15.82	5.33	4.9866	Y: DLA	20.9 ± 0.15
...	...	...	...	5.012	Y: subDLA	20.2 ± 0.2
J0747+1153	07:47:49.18	11:53:52.44	5.25	4.619	Y: subDLA	20.1 ± 0.2
...	...	...	...	5.1447	Y: DLA	21.1 ± 0.25
J0812+0440	08:12:48.82	04:40:56.57	5.31	5.108	Y: subDLA	20 ± 0.15
J0902+0851	09:02:45.76	08:51:15.90	5.21	4.586	Y: subDLA	19.3 ± 0.2
...	...	...	...	4.864	Y: subDLA	19.6 ± 0.2
...	...	...	...	5.070	Y: subDLA	19.8 ± 0.2
J1004+2025	10:04:44.31	20:25:20.03	5.00	4.854	Y: subDLA	20 ± 0.2
J1146+4037	11:46:57.79	40:37:08.59	4.98	4.533	Y: subDLA	19 ± 0.2
...	...	...	...	4.748	Y: subDLA	19.3 ± 0.1
J1147-0109	11:47:06.42	-01:09:58.37	5.25	5.062	Y: subDLA	19.6 ± 0.2
J1335-0328	13:35:56.24	-03:28:38.29	5.68	4.647	Y: subDLA	19.9 ± 0.2
...	...	...	...	5.295	Y: subDLA	19.7 ± 0.35
...	...	...	...	5.352	Y: subDLA	20.1 ± 0.2
J1345+2329	13:45:26.62	23:29:49.30	5.04	5.0060	N: Proximate DLA	21.1 ± 0.1
J1421+3433	14:21:03.83	34:33:32.00	4.94	4.665	Y: subDLA	20.2 ± 0.15
J1436+2132	14:36:05.00	21:32:39.26	5.22	5.1780	N: Proximate DLA	20.7 ± 0.25
J1443+3623	14:43:50.67	36:23:15.18	5.37	4.868	Y: subDLA	19.9 ± 0.2
J1523+3347	15:23:45.69	33:47:59.41	5.35	4.797	Y: subDLA	19.6 ± 0.2
J1534+1327	15:34:59.76	13:27:01.43	5.05	4.501	Y: subDLA	19.5 ± 0.3
...	...	...	...	4.961	N: Proximate subDLA	19.9 ± 0.3
J1601-1828	16:01:11.17	-18:28:35.07	5.03	5.052	N: Proximate subDLA	19.0 ± 0.1
J2202+1509	22:02:26.77	15:09:52.37	5.07	4.948	Y: subDLA	19.7 ± 0.15
J2207-0416	22:07:10.13	-04:16:56.22	5.51	4.7220	Y: DLA	20.4 ± 0.2
...	...	...	...	4.943	Y: subDLA	19.8 ± 0.2
...	...	...	...	5.036	Y: subDLA	20.0 ± 0.2
...	...	...	...	5.141	Y: subDLA	19.5 ± 0.3
...	...	...	...	5.3374	Y: DLA	20.8 ± 0.15
J2226-0618	22:26:12.42	−06:18:07.35	5.09	4.726	Y: subDLA	19.7 ± 0.2
J2325-0553	23:25:36.64	−05:53:28.42	5.20	4.940	Y: subDLA	20.1 ± 0.2
J2351-0459	23:51:24.31	−04:59:07.30	5.26	5.063	Y: subDLA	20.0 ± 0.2
J2358+0634	23:58:24.05	06:34:37.48	5.27	4.905	Y: subDLA	19.7 ± 0.2

Appendix C
$\rho_{\rm H\,I}$ Values

The observational constraints on $\rho_{\rm H\,I}$ used throughout this paper are reported in Table 5. Values were adapted to $H_0 = 70\,{\rm km\,s^{-1}\,Mpc^{-1}}$. We also assume $\delta_{\rm H\,I} = 1.2$ for all DLA measurements, except for Qz5 ($\delta_{\rm H\,I} = 1.44$). Any corrections for the contribution from Helium (e.g., C. Péroux & J. C. Howk 2020) were reversed.

Table 5
$\rho_{\rm H\,I}$ Values Used in This Paper

z	$z_{\rm bin}$	$\rho_{\rm H\,I} \times 10^{-8}$ ($M_\odot$ Mpc^{-3})	$\rho_{\rm H\,I} \times 10^{-8}(1\sigma)$ ($M_\odot$ Mpc^{-3})	Original References	Method	Retrieved from
0	(0, 0)	0.46	(0.38, 0.54)	M. A. Zwaan et al. (2005)	21 cm	F. Walter et al. (2020)
0	(0, 0)	0.79	(0.66, 0.92)	R. Braun (2012)	21 cm	F. Walter et al. (2020)
0.03	(0, 0.06)	0.39	(0.32, 0.46)	M. G. Jones et al. (2018)	21 cm	F. Walter et al. (2020)
0.03	(0, 0.04)	0.50	(0.45, 0.60)	J. Delhaize et al. (2013)	21 cm	F. Walter et al. (2020)
0.1	(0.04, 0.13)	0.56	(0.48, 0.66)	J. Delhaize et al. (2013)	21 cm	F. Walter et al. (2020)
0.07	(0, 0.12)	0.28	(0.20, 0.37)	L. Hoppmann et al. (2015)	21 cm	F. Walter et al. (2020)
0.1	(0.08, 0.12)	0.41	(0.35, 0.47)	J. Rhee et al. (2013)	21 cm	F. Walter et al. (2020)
0.2	(0.16, 0.22)	0.42	(0.32, 0.53)	J. Rhee et al. (2013)	21 cm	F. Walter et al. (2020)
0.24	(0.24, 0.24)	0.85	(0.48, 1.23)	P. Lah et al. (2007)	21 cm	F. Walter et al. (2020)
0.34	(0.2, 0.4)	0.48	(0.41, 0.55)	A. Bera et al. (2019)	21 cm	F. Walter et al. (2020)
1.06	(0.74, 1.45)	0.61	(0.46, 0.76)	A. Chowdhury et al. (2020)	21 cm	A. Chowdhury et al. (2020)
1.27	(1.18, 1.34)	<0.27[a]	(0.00, 0.09)	N. Kanekar et al. (2016)	21 cm	F. Walter et al. (2020)
0.41	(0, 0.69)	0.50	(0.32, 0.67)	K. Grasha et al. (2020)	21 cm abs.	K. Grasha et al. (2020)
1.1	(0.69, 2.74)	1.61	(0.81, 2.42)	K. Grasha et al. (2020)	21 cm abs.	K. Grasha et al. (2020)
0.46	(0.11, 0.61)	1.02	(0.68, 1.37)	S. M. Rao et al. (2017)	Mg II	F. Walter et al. (2020)
0.73	(0.61, 0.89)	0.89	(0.67, 1.10)	S. M. Rao et al. (2017)	Mg II	F. Walter et al. (2020)
1.17	(0.89, 1.65)	1.00	(0.61, 1.38)	S. M. Rao et al. (2017)	Mg II	F. Walter et al. (2020)
0.62	(0.01, 1.6)	0.30	(0.16, 0.54)	M. Neeleman et al. (2016)	DLAs	F. Walter et al. (2020)[a]
1.84	(1.51, 2)	1.05	(0.81, 1.28)	T. Zafar et al. (2013)	DLAs[b]	C. Péroux & J. C. Howk (2020)[b]
2.27	(2, 2.5)	1.13	(0.85, 1.40)	T. Zafar et al. (2013)	DLAs[b]	C. Péroux & J. C. Howk (2020)[b]
2.73	(2.5, 3)	1.21	(0.94, 1.48)	T. Zafar et al. (2013)	DLAs[b]	C. Péroux & J. C. Howk (2020)[b]
3.25	(3, 3.5)	1.26	(0.99, 1.53)	T. Zafar et al. (2013)	DLAs[b]	C. Péroux & J. C. Howk (2020)[b]
3.77	(3.5, 4)	0.95	(0.75, 1.15)	T. Zafar et al. (2013)	DLAs[b]	C. Péroux & J. C. Howk (2020)[b]
4.2	(4, 5)	0.96	(0.73, 1.20)	T. Zafar et al. (2013)	DLAs[b]	C. Péroux & J. C. Howk (2020)[b]
2.14	(1.55, 2.73)	1.97	(1.17, 3.15)	R. Sánchez-Ramírez et al. (2016)	DLAs	F. Walter et al. (2020)
2.97	(2.73, 3.21)	0.73	(0.38, 1.31)	R. Sánchez-Ramírez et al. (2016)	DLAs	F. Walter et al. (2020)
2.15	(2, 2.3)	1.31	(1.25, 1.38)	P. Noterdaeme et al. (2012)	DLAs	F. Walter et al. (2020)
2.45	(2.3, 2.6)	1.15	(1.10, 1.21)	P. Noterdaeme et al. (2012)	DLAs	F. Walter et al. (2020)
2.75	(2.6, 2.9)	1.38	(1.32, 1.45)	P. Noterdaeme et al. (2012)	DLAs	F. Walter et al. (2020)
3.05	(2.9, 3.2)	1.46	(1.36, 1.56)	P. Noterdaeme et al. (2012)	DLAs	F. Walter et al. (2020)
3.35	(3.2, 3.5)	1.69	(1.51, 1.86)	P. Noterdaeme et al. (2012)	DLAs	F. Walter et al. (2020)
2.31	(2.2, 2.4)	0.68	(0.56, 0.80)	J. X. Prochaska & A. M. Wolfe (2009)	DLAs	F. Walter et al. (2020)
2.57	(2.4, 2.7)	0.92	(0.82, 1.02)	J. X. Prochaska & A. M. Wolfe (2009)	DLAs	F. Walter et al. (2020)
2.86	(2.7, 3.0)	0.92	(0.83, 1.02)	J. X. Prochaska & A. M. Wolfe (2009)	DLAs	F. Walter et al. (2020)
3.22	(3, 3.5)	1.29	(1.18, 1.40)	J. X. Prochaska & A. M. Wolfe (2009)	DLAs	F. Walter et al. (2020)
2.35	(2, 2.7)	1.34	(1.06, 1.65)	C. Péroux et al. (2003)	DLAs	F. Walter et al. (2020)
3.1	(2.7, 3.5)	1.23	(0.95, 1.55)	C. Péroux et al. (2003)	DLAs	F. Walter et al. (2020)
3.9	(3.5, 4.85)	0.76	(0.51, 1.03)	C. Péroux et al. (2003)	DLAs	F. Walter et al. (2020)
2.44	(2.23, 2.6)	1.03	(0.94, 1.12)	P. Noterdaeme et al. (2009)	DLAs	C. Péroux & J. C. Howk (2020)
2.74	(2.6, 2.88)	1.06	(0.98, 1.15)	P. Noterdaeme et al. (2009)	DLAs	C. Péroux & J. C. Howk (2020)
3.02	(2.88, 3.2)	1.29	(1.19, 1.39)	P. Noterdaeme et al. (2009)	DLAs	C. Péroux & J. C. Howk (2020)
3.17	(2.55, 3.4)	1.37	(0.90, 1.98)	R. Guimarães et al. (2009)	DLAs	F. Walter et al. (2020)
3.62	(3.4, 3.83)	1.21	(0.79, 1.68)	R. Guimarães et al. (2009)	DLAs	F. Walter et al. (2020)
4.05	(3.83, 5.03)	1.07	(0.68, 1.55)	R. Guimarães et al. (2009)	DLAs	F. Walter et al. (2020)
3.82	(3.5, 4.3)	1.12	(0.91, 1.33)	A. Songaila & L. L. Cowie (2010)	DLAs	N. H. M. Crighton et al. (2015)
4.45	(4.3, 5.1)	1.05	(0.55, 1.76)	A. Songaila & L. L. Cowie (2010)	DLAs	N. H. M. Crighton et al. (2015)
4.01	(3.56, 4.45)	1.73	(1.36, 2.11)	N. H. M. Crighton et al. (2015)	DLAs	F. Walter et al. (2020)
4.88	(4.45, 5.31)	1.44	(1.19, 1.73)	N. H. M. Crighton et al. (2015)	DLAs	F. Walter et al. (2020)
4.99	(4.5, 5.57)	0.56	(0.31, 0.82)	This work	DLAs[b]	This work

Notes.
[a] This upper limit corresponds to 3σ (N. Kanekar et al. 2016).
[b] These studies include direct measurements of the contribution from subDLAs.

ORCID iDs

Grecco A. Oyarzún https://orcid.org/0000-0003-0028-4130
Marc Rafelski https://orcid.org/0000-0002-9946-4731
Lise Christensen https://orcid.org/0000-0001-8415-7547
Regina A. Jorgenson https://orcid.org/0000-0003-2973-0472
M. Neeleman https://orcid.org/0000-0002-9838-8191
Michele Fumagalli https://orcid.org/0000-0001-6676-3842
J. Xavier Prochaska https://orcid.org/0000-0002-7738-6875
G. Worseck https://orcid.org/0000-0003-0960-3580
M. E. Wisz https://orcid.org/0000-0002-6505-9981
George D. Becker https://orcid.org/0000-0003-2344-263X
Sebastián López https://orcid.org/0000-0003-0389-0902

References

Adelman-McCarthy, J. K., Agüeros, M. A., Allam, S. S., et al. 2007, ApJS, 172, 634
Ahn, C. P., Alexandroff, R., Allende Prieto, C., et al. 2014, ApJS, 211, 17
Astropy Collaboration, Price-Whelan, A. M., Lim, P. L., et al. 2022, ApJ, 935, 167
Astropy Collaboration, Price-Whelan, A. M., Sipőcz, B. M., et al. 2018, AJ, 156, 123
Astropy Collaboration, Robitaille, T. P., Tollerud, E. J., et al. 2013, A&A, 558, A33
Bahcall, J. N., & Peebles, P. J. E. 1969, ApJL, 156, L7
Balashev, S. A., Noterdaeme, P., Rahmani, H., et al. 2017, MNRAS, 470, 2890
Becker, G. D., Bolton, J. S., Madau, P., et al. 2015, MNRAS, 447, 3402
Begum, A., Chengalur, J. N., Karachentsev, I. D., Sharina, M. E., & Kaisin, S. S. 2008, MNRAS, 386, 1667
Bera, A., Kanekar, N., Chengalur, J. N., & Bagla, J. S. 2019, ApJL, 882, L7
Berg, T. A. M., Ellison, S. L., Prochaska, J. X., et al. 2017, MNRAS, 464, L56
Berg, T. A. M., Ellison, S. L., Sánchez-Ramírez, R., et al. 2019, MNRAS, 488, 4356
Berry, M., Somerville, R. S., Gawiser, E., et al. 2016, MNRAS, 458, 531
Berry, M., Somerville, R. S., Haas, M. R., et al. 2014, MNRAS, 441, 939
Bigiel, F., Leroy, A., Walter, F., et al. 2008, AJ, 136, 2846
Bird, S., Garnett, R., & Ho, S. 2017, MNRAS, 466, 2111
Bolmer, J., Ledoux, C., Wiseman, P., et al. 2019, A&A, 623, A43
Bosman, S. E. I., Davies, F. B., Becker, G. D., et al. 2022, MNRAS, 514, 55
Bosman, S. E. I., Fan, X., Jiang, L., et al. 2018, MNRAS, 479, 1055
Bouché, N., Dekel, A., Genzel, R., et al. 2010, ApJ, 718, 1001
Braun, R. 2012, ApJ, 749, 87
Byrohl, C., Nelson, D., Behrens, C., et al. 2021, MNRAS, 506, 5129
Catinella, B., Saintonge, A., Janowiecki, S., et al. 2018, MNRAS, 476, 875
Catinella, B., Schiminovich, D., Cortese, L., et al. 2013, MNRAS, 436, 34
Chen, H.-W., & Lanzetta, K. M. 2003, ApJ, 597, 706
Chowdhury, A., Kanekar, N., & Chengalur, J. N. 2022, ApJ, 937, 103
Chowdhury, A., Kanekar, N., Chengalur, J. N., Sethi, S., & Dwarakanath, K. S. 2020, Natur, 586, 369
Chowdhury, A., Kanekar, N., Das, B., Dwarakanath, K. S., & Sethi, S. 2021, ApJL, 913, L24
Christensen, L., Møller, P., Fynbo, J. P. U., & Zafar, T. 2014, MNRAS, 445, 225
Combes, F., & Gupta, N. 2024, A&A, 683, A20
Crighton, N. H. M., Murphy, M. T., Prochaska, J. X., et al. 2015, MNRAS, 452, 217
Davé, R., Anglés-Alcázar, D., Narayanan, D., et al. 2019, MNRAS, 486, 2827
Dawson, K. S., Schlegel, D. J., Ahn, C. P., et al. 2013, AJ, 145, 10
Delhaize, J., Meyer, M. J., Staveley-Smith, L., & Boyle, B. J. 2013, MNRAS, 433, 1398
Dou, J., Peng, Y., Gu, Q., et al. 2024, ApJL, 973, L23
Ellison, S. L., Prochaska, J. X., Hennawi, J., et al. 2010, MNRAS, 406, 1435
Ellison, S. L., Prochaska, J. X., & Mendel, J. T. 2011, MNRAS, 412, 448
Fall, S. M., Charlot, S., & Pei, Y. C. 1996, ApJL, 464, L43
Fall, S. M., & Pei, Y. C. 1993, ApJ, 402, 479
Fall, S. M., Pei, Y. C., & McMahon, R. G. 1989, ApJL, 341, L5
Fernández, X., Gim, H. B., van Gorkom, J. H., et al. 2016, ApJL, 824, L1
Fraternali, F., van Moorsel, G., Sancisi, R., & Oosterloo, T. 2002, AJ, 123, 3124
Fumagalli, M., Mackenzie, R., Trayford, J., et al. 2017, MNRAS, 471, 3686
Fynbo, J. P. U., Laursen, P., Ledoux, C., et al. 2010, MNRAS, 408, 2128
Glover, S. C. O., & Clark, P. C. 2012, MNRAS, 421, 9
Grasha, K., Darling, J., Leroy, A. K., & Bolatto, A. D. 2020, MNRAS, 498, 883
Grazian, A., Boutsia, K., Giallongo, E., et al. 2023, ApJ, 955, 60
Guimarães, R., Petitjean, P., de Carvalho, R. R., et al. 2009, A&A, 508, 133
Hamanowicz, A., Péroux, C., Zwaan, M. A., et al. 2020, MNRAS, 492, 2347
Haynes, M. P., & Giovanelli, R. 1984, AJ, 89, 758
Haynes, M. P., Giovanelli, R., Kent, B. R., et al. 2018, ApJ, 861, 49
Heintz, K. E., Oesch, P. A., Aravena, M., et al. 2022, ApJL, 934, L27
Heintz, K. E., Watson, D., Brammer, G., et al. 2024, Sci, 384, 890
Henriques, B. M. B., Yates, R. M., Fu, J., et al. 2020, MNRAS, 491, 5795
Ho, M.-F., Bird, S., & Garnett, R. 2020, MNRAS, 496, 5436
Hoppmann, L., Staveley-Smith, L., Freudling, W., et al. 2015, MNRAS, 452, 3726
Jones, M. G., Haynes, M. P., Giovanelli, R., & Moorman, C. 2018, MNRAS, 477, 2
Jorgenson, R. A., & Wolfe, A. M. 2014, ApJ, 785, 16
Kanekar, N., Prochaska, J. X., Neeleman, M., et al. 2020, ApJL, 901, L5
Kanekar, N., Sethi, S., & Dwarakanath, K. S. 2016, ApJL, 818, L28
Kaur, B., Kanekar, N., Rafelski, M., et al. 2021, ApJ, 921, 68
Kaur, B., Kanekar, N., Rafelski, M., et al. 2022a, ApJL, 933, L42
Kaur, B., Kanekar, N., Revalski, M., et al. 2022b, ApJ, 934, 87
Kennicutt, R. C. 1998, ARA&A, 36, 189
Kennicutt, R. C., & Evans, N. J. 2012, ARA&A, 50, 531
Krogager, J. K., Møller, P., Fynbo, J. P. U., & Noterdaeme, P. 2017, MNRAS, 469, 2959
Krumholz, M. R. 2012, ApJ, 759, 9
Krumholz, M. R., Leroy, A. K., & McKee, C. F. 2011, ApJ, 731, 25
Lagos, C. D. P., Baugh, C. M., Zwaan, M. A., et al. 2014, MNRAS, 440, 920
Lah, P., Chengalur, J. N., Briggs, F. H., et al. 2007, MNRAS, 376, 1357
Lanzetta, K. M., Wolfe, A. M., Turnshek, D. A., et al. 1991, ApJS, 77, 1
Leroy, A. K., Walter, F., Brinks, E., et al. 2008, AJ, 136, 2782
Lofthouse, E. K., Fumagalli, M., Fossati, M., et al. 2023, MNRAS, 518, 305
López, S., D'Odorico, V., Ellison, S. L., et al. 2016, A&A, 594, A91
Mackenzie, R., Fumagalli, M., Theuns, T., et al. 2019, MNRAS, 487, 5070
Madau, P., & Dickinson, M. 2014, ARA&A, 52, 415
Maio, U., Péroux, C., & Ciardi, B. 2022, A&A, 657, A47
Martindale, H., Thomas, P. A., Henriques, B. M., & Loveday, J. 2017, MNRAS, 472, 1981
Matejek, M. S., & Simcoe, R. A. 2012, ApJ, 761, 112
Modigliani, A., Goldoni, P., & Royer, F. 2010, Proc. SPIE, 7737, 773728
Møller, P., & Warren, S. J. 1993, A&A, 270, 43
Murphy, M. T., & Bernet, M. L. 2016, MNRAS, 455, 1043
Napolitano, L., Myers, A. D., Aguilar, J., et al. 2024, arXiv:2412.15383
Neeleman, M., Kanekar, N., Prochaska, J. X., et al. 2017, Sci, 355, 1285
Neeleman, M., Kanekar, N., Prochaska, J. X., et al. 2018, ApJL, 856, L12
Neeleman, M., Kanekar, N., Prochaska, J. X., Rafelski, M. A., & Carilli, C. L. 2019, ApJL, 870, L19
Neeleman, M., Prochaska, J. X., Ribaudo, J., et al. 2016, ApJ, 818, 113
Neeleman, M., Prochaska, J. X., & Wolfe, A. M. 2015, ApJ, 800, 7
Neeleman, M., Wolfe, A. M., Prochaska, J. X., & Rafelski, M. 2013, ApJ, 769, 54
Noterdaeme, P., Balashev, S., Cuellar, R., et al. 2023, A&A, 673, A89
Noterdaeme, P., Petitjean, P., Carithers, W. C., et al. 2012, A&A, 547, L1
Noterdaeme, P., Petitjean, P., Ledoux, C., & Srianand, R. 2009, A&A, 505, 1087
Noterdaeme, P., Petitjean, P., & Srianand, R. 2015, A&A, 578, L5
Oke, J. B., & Gunn, J. E. 1983, ApJ, 266, 713
O'Meara, J. M., Prochaska, J. X., Burles, S., et al. 2007, ApJ, 656, 666
Oyarzún, G. A., Rafelski, M., Kanekar, N., et al. 2024, ApJ, 962, 72
Pâris, I., Petitjean, P., Ross, N. P., et al. 2017, A&A, 597, A79
Pei, Y. C., & Fall, S. M. 1995, ApJ, 454, 69
Pei, Y. C., Fall, S. M., & Bechtold, J. 1991, ApJ, 378, 6
Pei, Y. C., Fall, S. M., & Hauser, M. G. 1999, ApJ, 522, 604
Péroux, C., & Howk, J. C. 2020, ARA&A, 58, 363
Péroux, C., McMahon, R. G., Storrie-Lombardi, L. J., & Irwin, M. J. 2003, MNRAS, 346, 1103
Popping, G., Pillepich, A., Somerville, R. S., et al. 2019, ApJ, 882, 137
Popping, G., Somerville, R. S., & Trager, S. C. 2014, MNRAS, 442, 2398
Prochaska, J. X., Gawiser, E., Wolfe, A. M., Cooke, J., & Gelino, D. 2003, ApJS, 147, 227
Prochaska, J. X., Hennawi, J. F., & Herbert-Fort, S. 2008, ApJ, 675, 1002
Prochaska, J. X., Hennawi, J. F., Lee, K.-G., et al. 2013, ApJ, 776, 136
Prochaska, J. X., Herbert-Fort, S., & Wolfe, A. M. 2005, ApJ, 635, 123
Prochaska, J. X., Neeleman, M., Kanekar, N., & Rafelski, M. 2019, ApJL, 886, L35
Prochaska, J. X., O'Meara, J. M., & Worseck, G. 2010, ApJ, 718, 392
Prochaska, J. X., Tejos, N., Crighton, N., et al. 2016, linetools/linetools: Second major release, v0.2, Zenodo, doi:10.5281/zenodo.168270
Prochaska, J. X., & Wolfe, A. M. 1997, ApJ, 487, 73
Prochaska, J. X., & Wolfe, A. M. 2009, ApJ, 696, 1543
Qin, Y., Mesinger, A., Bosman, S. E. I., & Viel, M. 2021, MNRAS, 506, 2390
Rafelski, M., Neeleman, M., Fumagalli, M., Wolfe, A. M., & Prochaska, J. X. 2014, ApJL, 782, L29
Rafelski, M., Wolfe, A. M., Prochaska, J. X., Neeleman, M., & Mendez, A. J. 2012, ApJ, 755, 89
Rahmati, A., Schaye, J., Bower, R. G., et al. 2015, MNRAS, 452, 2034
Rao, S. M., Turnshek, D. A., Sardane, G. M., & Monier, E. M. 2017, MNRAS, 471, 3428
Rhee, J., Zwaan, M. A., Briggs, F. H., et al. 2013, MNRAS, 435, 2693
Rhodin, N. H. P., Krogager, J. K., Christensen, L., et al. 2021, MNRAS, 506, 546
Rodríguez-Puebla, A., Behroozi, P., Primack, J., et al. 2016, MNRAS, 462, 893

Sánchez-Ramírez, R., Ellison, S. L., Prochaska, J. X., et al. 2016, MNRAS, 456, 4488
Sancisi, R., Fraternali, F., Oosterloo, T., & van der Hulst, T. 2008, A&ARv, 15, 189
Sharma, A., Masters, K. L., Stark, D. V., et al. 2023, MNRAS, 526, 1573
Sheinis, A. I., Bolte, M., Epps, H. W., et al. 2002, PASP, 114, 851
Shull, J. M., Danforth, Ch. W., Tilton, E. M., Moloney, J., & Stevans, M. L. 2017, ApJ, 849, 106
Smette, A., Sana, H., Noll, S., et al. 2015, A&A, 576, A77
Somerville, R. S., Gilmore, R. C., Primack, J. R., & Domìnguez, A. 2012, MNRAS, 423, 1992
Somerville, R. S., Hopkins, P. F., Cox, T. J., Robertson, B. E., & Hernquist, L. 2008, MNRAS, 391, 481
Somerville, R. S., & Primack, J. R. 1999, MNRAS, 310, 1087
Somerville, R. S., Primack, J. R., & Faber, S. M. 2001, MNRAS, 320, 504
Songaila, A., & Cowie, L. L. 2010, ApJ, 721, 1448
Spina, B., Bosman, S. E. I., Davies, F. B., Gaikwad, P., & Zhu, Y. 2024, A&A, 688, L26
Spinelli, M., Zoldan, A., De Lucia, G., Xie, L., & Viel, M. 2020, MNRAS, 493, 5434
Stern, J., Fielding, D., Hafen, Z., et al. 2024, MNRAS, 530, 1711
Stern, J., Sternberg, A., Faucher-Giguère, C.-A., et al. 2021, MNRAS, 507, 2869
Sun, Z., Ting, Y.-S., & Cai, Z. 2023, ApJS, 269, 4
Tacconi, L. J., Genzel, R., Saintonge, A., et al. 2018, ApJ, 853, 179
Theuns, T. 2021, MNRAS, 500, 2741
Tumlinson, J., Peeples, M. S., & Werk, J. K. 2017, ARA&A, 55, 389
Vernet, J., Dekker, H., D'Odorico, S., et al. 2011, A&A, 536, A105
Villaescusa-Navarro, F., Genel, S., Castorina, E., et al. 2018, ApJ, 866, 135
Vogelsberger, M., Genel, S., Springel, V., et al. 2014, MNRAS, 444, 1518
Walter, F., Brinks, E., de Blok, W. J. G., et al. 2008, AJ, 136, 2563
Walter, F., Carilli, C., Neeleman, M., et al. 2020, ApJ, 902, 111
Wang, F., Wu, X.-B., Fan, X., et al. 2016, ApJ, 819, 24
Wang, J., Koribalski, B. S., Serra, P., et al. 2016, MNRAS, 460, 2143
Wolfe, A. M., Gawiser, E., & Prochaska, J. X. 2005, ARA&A, 43, 861
Wolfe, A. M., Lanzetta, K. M., Foltz, C. B., & Chaffee, F. H. 1995, ApJ, 454, 698
Worseck, G., Prochaska, J. X., O'Meara, J. M., et al. 2014, MNRAS, 445, 1745
Wright, E. L., Eisenhardt, P. R. M., Mainzer, A. K., et al. 2010, AJ, 140, 1868
Xi, H., Peng, B., Staveley-Smith, L., et al. 2024, ApJL, 966, L36
Yang, J., Wang, F., Wu, X.-B., et al. 2016, ApJ, 829, 33
Yates, R. M., Péroux, C., & Nelson, D. 2021, MNRAS, 508, 3535
Yu, N., Ho, L. C., & Wang, J. 2022, ApJ, 930, 85
Zafar, T., Péroux, C., Popping, A., et al. 2013, A&A, 556, A141
Zhu, Y., Becker, G. D., Bosman, S. E. I., et al. 2024, MNRAS, 533, L49
Zhu, Y., Becker, G. D., Christenson, H. M., et al. 2023, ApJ, 955, 115
Zwaan, M. A., Meyer, M. J., Staveley-Smith, L., & Webster, R. L. 2005, MNRAS, 359, L30